Wake Characterization of a Cross-Flow Turbine

Chase Haegele

A thesis
submitted in partial fulfillment of the
requirements for the degree of

Master of Science in Mechanical Engineering

University of Washington

2014

Reading Committee:

Brian Polagye, Chair

Alberto Aliseda

Andy Stewart

Program Authorized to Offer Degree:
Mechanical Engineering

University of Washington

Abstract

Wake Characterization of a Cross-Flow Turbine

Chase Haegele

Chair of the Supervisory Committee:
Assistant Professor Brian Polagye
Department of Mechanical Engineering

A cross-flow turbine wake is analyzed to better understand how these turbines affect the flow field in their immediate vicinity. Mean velocity, turbulence intensity, coherent turbulent kinetic energy, and Reynolds shear stresses are used to identify regions of turbulence and mixing. The shear layer between the turbine wake and bypass flow resembles a rectangular ring near the turbine which grows into a larger oval downstream. Mixing allows the wake to recover to roughly 70% of the free stream velocity at five diameters downstream. The results of this study gives future researchers a map to locate areas of interest for more in depth research.

TABLE OF CONTENTS

LIST OF FIGURES

NOMENCLATURE

b: Flume width.

L: Flume working length.

H_{surf}: Flume water surface height.

ϕ: Doppler phase shift angle.

T_{ij}: ADV beam transformation matrix coefficient.

b_i: ADV beam measurement.

u_i: Water velocity transformed from ADV beam coordinates.

u: Stream-wise velocity.

v: Cross-stream velocity.

w: Vertical velocity.

U: Vector sum velocity.

u_i': Perturbation velocity.

$\overline{u_i}$: Mean velocity.

u_i: Instantaneous velocity.

I_u: Stream-wise turbulence intensity.

I_v: Cross-stream turbulence intensity.

I_w: Vertical turbulence intensity.

I_U: Turbulence intensity of velocity magnitude.

ρ: Density.

ACKNOWLEDGMENTS

The author wishes to express sincere appreciation to the Alice C. Tyler Trust for funding the Gantry and the authors education. He would also like to thank Dr. Brian Polagye and everyone in the Marine Renewable Energy Lab for their inspiration and support.

Chapter 1
INTRODUCTION

Gravitational interactions between the earth, sun, and moon produce predictable ocean tides. In response to these tides, water flowing in and out of narrow inlets or bays can create high velocity currents. These are areas for potential energy generation by marine hydrokinetic turbines that harness the power of the moving water. Like wind turbines, marine hydrokinetic turbines can be deployed as single devices or as arrays.

In 2010, the average electrical consumption was 444 GW [14]. The sun and moon put 3.5 TW of power into the earths tides, of which a small fraction could likely be harnessed to produce electricity. While not a silver bullet, it is important to consider all forms of renewable energy to reduce our reliance on fossil fuels. In particular, marine hydrokinetic energy has the potential to be a valuable additional energy source for small communities located far from large power production plants or other fuel sources.

Marine hydrokinetic turbines can be divided into two primary categories: axial flow and cross flow turbines. Axial flow turbines, an example of which is shown in Figure 1.1, operate with the fluid flow in the direction of the rotational axis and, have become the dominant turbine design in the wind energy field. Cross-flow turbines harness energy as fluid flows across the axis of the turbine rotation, an example of which is shown in Figure 1.2. Although, cross-flow turbines typically have lower energy efficiency, they are particularly useful in marine environments because they are insensitive to incoming flow direction when mounted with a vertical axis of rotation and have a form factor amenable to high-blockage arrays.

Figure 1.1: Verdant Power axial flow turbine [2].

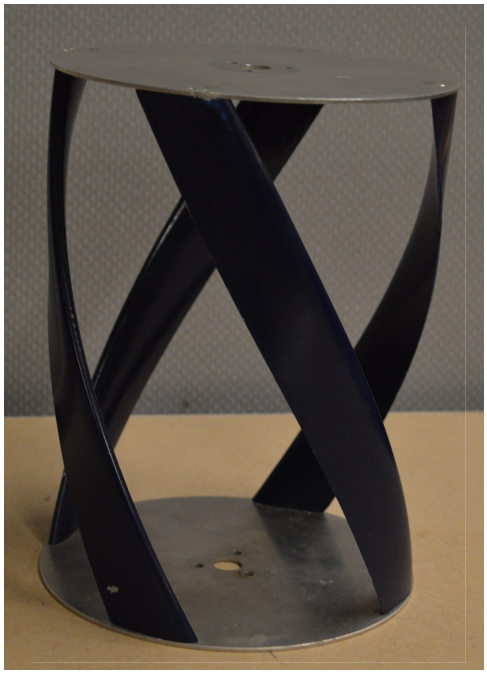

Figure 1.2: Vertical axis helical blade cross-flow turbine.

A scale model of a vertical axis cross-flow turbine, developed by the Marine Renewable

Energy Laboratory (MREL), at the University of Washington, was tested in a laboratory flume to characterize its performance and wake structure in a controlled environment. Understanding wake recovery will allow for optimized turbine array spacing and improve overall array efficiency.

1.1 Previous Work

Previous work has shown that optimizing turbine spacing in an array can increase performance. For example, Archer et al. (2013) used a large eddy simulation of turbines (represented as actuator lines) to demonstrate that array layout optimization could improve overall performance by 13-33%. As one might expect, the configuration with the largest spacing in the direction of the wind had the lowest array losses and highest capacity factor.

Looking more specifically at cross-flow turbines, Li and Calisal (2010) analyze the combined performance of two cross-flow turbines varying the distance between turbines, rotation direction, and incoming flow angle. The turbines consisted of three straight blades and were operated at tip speed ratios from 4.25 to 5.25 as counter-rotating and co-rotating pairs. Numerical simulations and experimental results both found that the overall system efficiency of two properly spaced turbines can be greater than two times the stand-alone efficiency of an individual turbine. The numerical predictions came within 10% of the experimental values. This demonstrates that turbine wake interactions are important but does not provide specific information about the wake structure.

Bachant and Wosnik (2013) analyzed a wake cross-section normal to the flow direction at one diameter downstream of a cross-flow turbine operating in a tow tank. A 1 m diameter, four straight NACA 0020 bladed turbine operating at an approximate blade chord Reynolds number of 10^5. For the wake characterization, the turbine was operating at a tip speed ratio of 1.9. They found that the stream-wise velocity had a sharp drop between the wake and bypass flow. Turbulence intensity in the stream-wise direction was concentrated on the periphery of the turbine swept area (Figure 1.3). The wake was also shifted in the positive y-direction because of the turbine rotation.

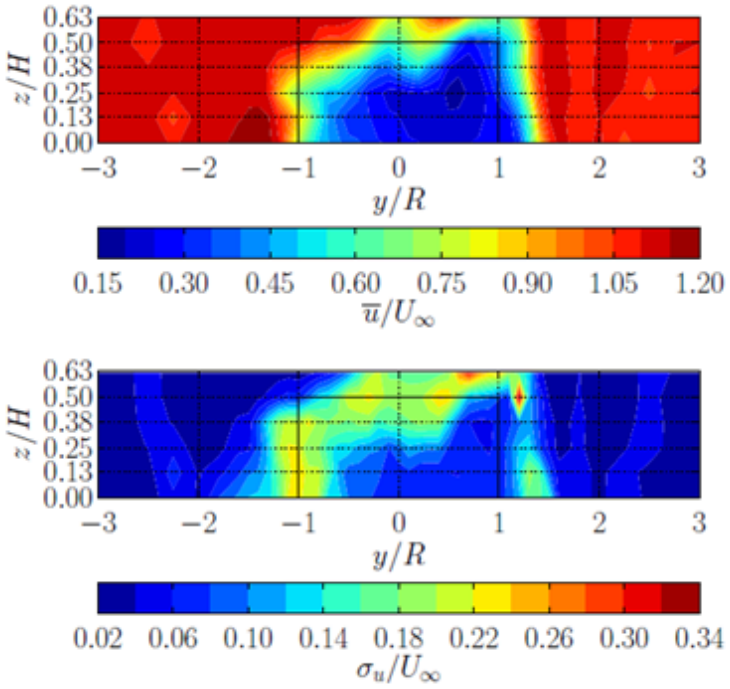

Figure 1.3: Stream-wise mean velocity and turbulence intensity [4].

Scheurich et al. (2011) used a Vorticity Transport Model to simulate the wake structure of a two blade NACA 0012 vertical axis turbine with an average blade Reynolds number of 40,000. Vortices are found in the wake as shown in (Figure 1.4).

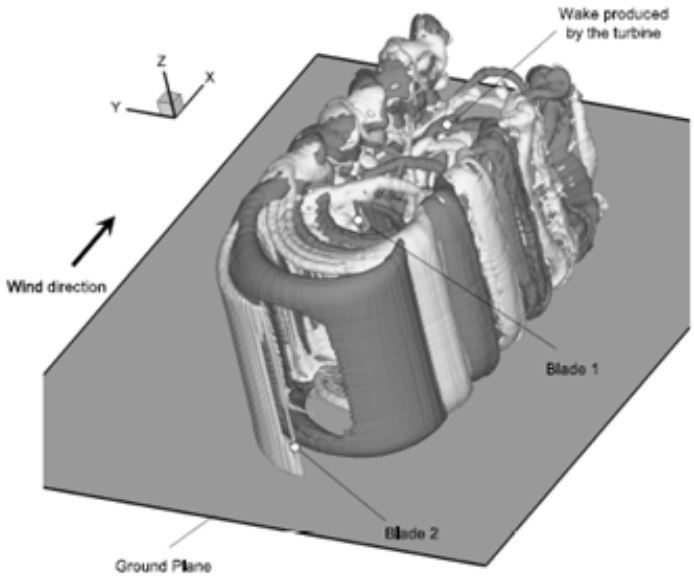

Figure 1.4: Propagating wake produced by the turbine [13].

Although this study models the near wake well, the far wake was modeled with a coarser grid, as shown in Figure 1.5. The goal of the study was to compare model vorticity and experimental blade stresses to numerical results and, therefore, the far wake was not of as much interest as close to the turbine. In Grid Level 3 the wake appears to contract and then expand again in Grid Level 4. This may occur once the vorticity breaks down and mixes with the surrounding flow, but the coarse grid increases uncertainty in the results.

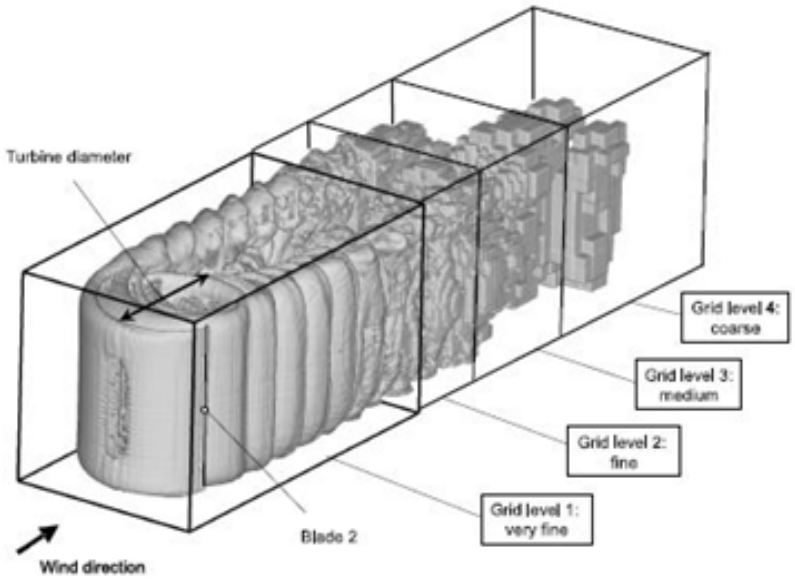

Figure 1.5: Turbine wake after 7 revolutions [13].

A cross-flow turbine with helical blades was tested by Niblick (2012) to determine coefficient of power, coefficient of torque, and efficiency under various test conditions. The turbine had a 17.2 cm diameter and NACA 0018 blades with a 60 degree helical pitch angle. Sparse wake measurements were also collected at the mid-plane of the turbine. These showed the stream-wise velocity recovered to about 50 percent of upstream water velocity at five rotor diameters downstream and 75 percent at 11.5 rotor diameters downstream.

Polagye et al. (2013) reported experimental wake data on a 72.4 cm diameter vertical axis cross-flow turbine. Turbulence intensity was found to be greatest directly behind the turbine, shown in Figure 1.6 by the dark blue dot for all three tow speeds. For the slowest speed, 1 m/s, the turbulence intensity has high magnitudes at many locations in the wake. It is also shown that the wake nearly fully recovered to the upstream velocity at ten diameters downstream (Figure 1.7).

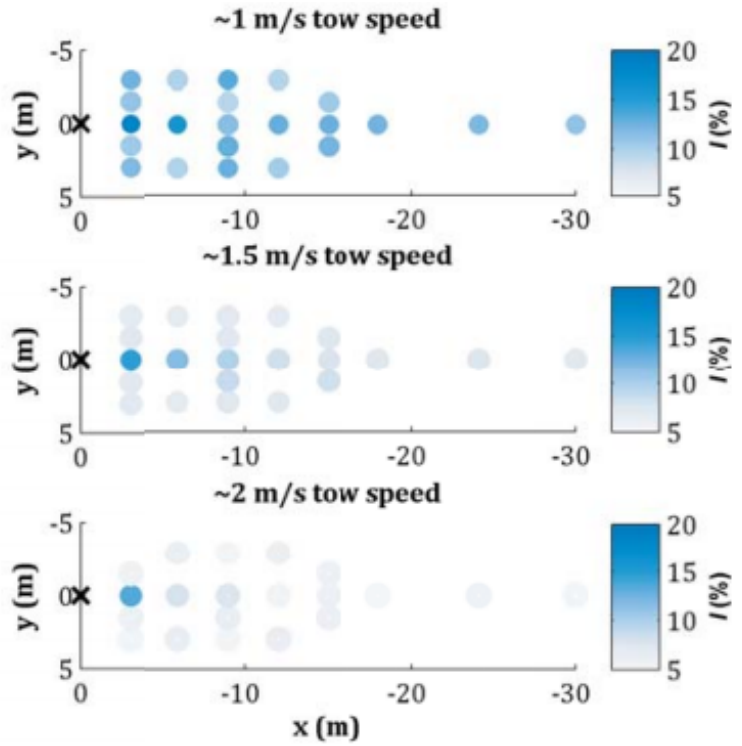

Figure 1.6: Turbulence as a function of tow speed [10].

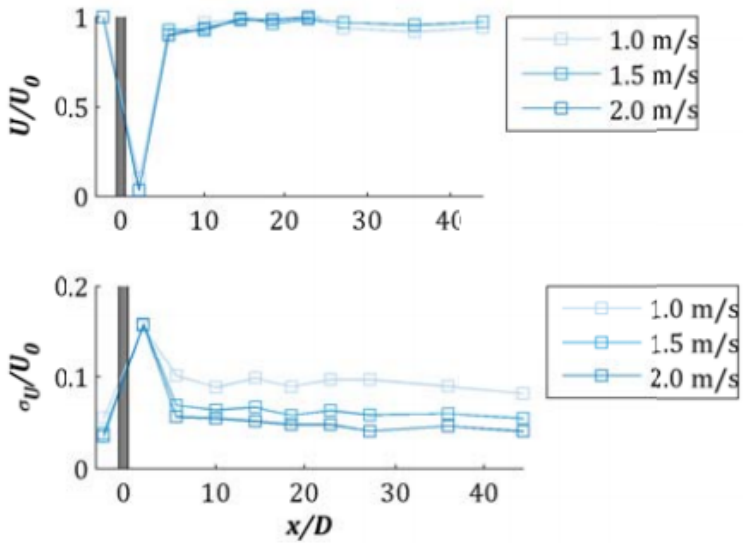

Figure 1.7: Mean wake velocity (top) and standard deviation of wake velocity (bottom). Turbine is located at $x/D = 0$ [10].

1.2 Project Motivation

The complete wake structure of cross-flow turbines plays an important role in array efficiency, but has not been studied thoroughly by experimentation. This is in sharp contrast to axial flow turbine wakes which have been well-documented because of their prevalence in the wind energy field.

This thesis investigates the wake structure of an experimental cross-flow turbine in a water flume. Flumes are commonly used test facilities for scale-turbine experiments. Despite the effects of blockage [5], flumes are superior to tow tanks. Flumes allow continuous operation, unlike tow tanks that need to be reset after each run, allowing more data to be collected over a shorter period of time.

In this study, acoustic Doppler velocimeters are chosen to record water velocity because of their relatively high sampling rate (100Hz). This higher resolution enables calculations of higher order statistics more easily than with a particle image velocimetery system. To accurately position velocimeters in the turbine wake, a three axis motion controlled gantry was designed, allowing automated control and repeatable testing with high spatial resolution.

Chapter 2

METHODS

2.1 Experimental Setup

2.1.1 Water Flume Experimental Facilities

The Bamfield Marine Science Centre (BMSC) flume in Bamfield, Canada was used for this study. An overhead view of a typical test set up is shown in Figure 2.1. The origin, is the coordinate systems adopted for this study, marked by the red axes at the turbine center, with the zero z-axis located at mid-plane of the turbine. Stream-wise and x-direction, cross-stream and y-direction, and vertical and z-direction will be used interchangeably.

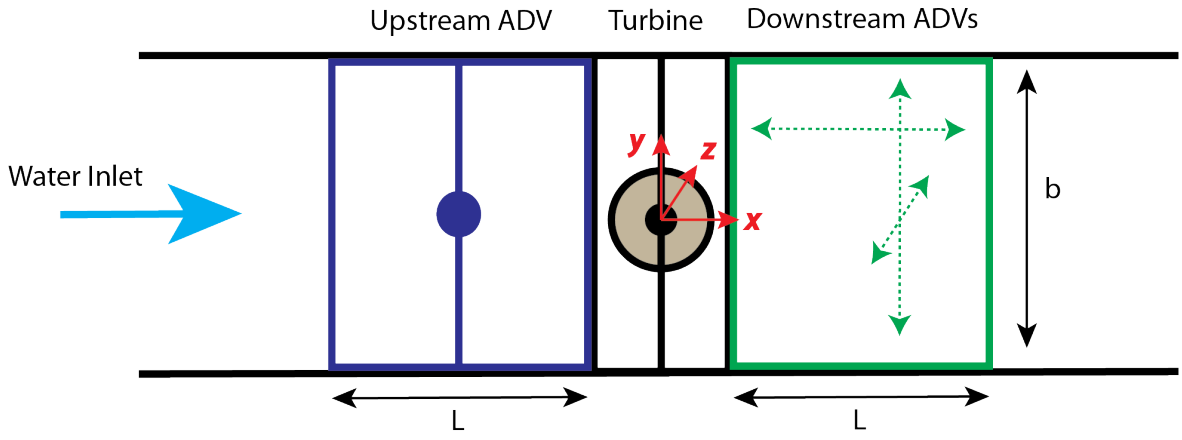

Figure 2.1: Flume dimensions and setup.

The motion-controlled gantry system was designed to for the flume width (b), working length (L), and water surface height (H_{surf}) as presented in Table 1. Peak velocity in the BMSC flume is 1 m/s with a mean turbulence intensity of 8%.

Dimensions (meters)	**BMSC**
b	1
L	2
H_{surf}	1

Table 2.1: BMSC Flume dimensions.

2.1.2 Downstream Instrumentation Gantry

To accurately, repeatably, and efficiently measure the cross-flow turbine wakes a motion-controlled gantry system was designed to position sensing instrumentation at a sequence of x-y-z positions. The gantry is capable of positioning instruments within a 1.5 x 0.9 x 1.11 m space, on the x-, y-, z- axes respectively. The underlying structure of the gantry consists of aluminum extrusions with the motion controlled by linear slides (Velmex Inc., Bloomfield, NY): two parallel coupled (x- and z-axis) and one single (y-axis). These have a repeatability of 4 x 10^{-6} m and a straight line accuracy of 0.076 mm over the entire travel distance [1]. Both the x and z axes have an additional passive carriage per slide to help reduce cantilever loads. Cantilever forces on the y-axis are reduced via a passive bearing mounted to a rail below the Velmex slide.

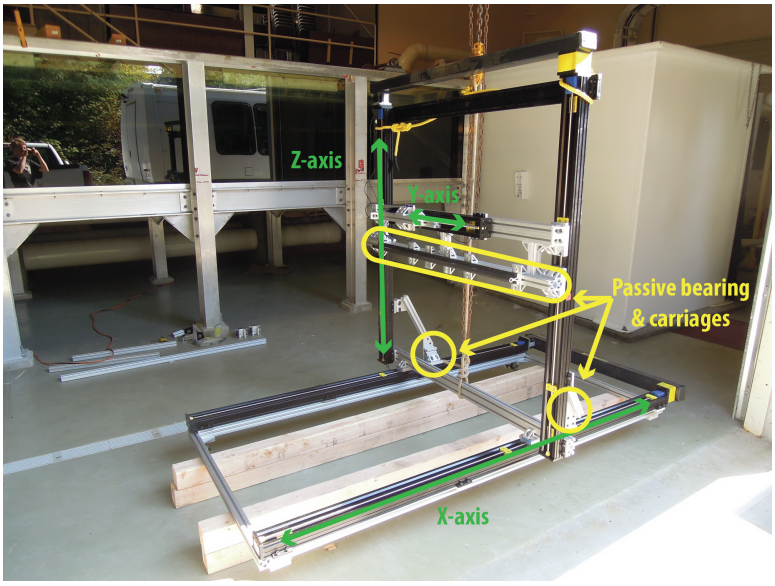

Figure 2.2: Fully assembled gantry.

2.1.3 Acoustic Doppler Velocimeters

Two Nortek Vectrino Profilers (Nortek AS, Norway), synchronized via a triggering pulse, were used to measure three-dimensional velocity. The Vectrino Profilers emit a 10 MHz acoustic signal which consists of a pair of pulses with a known time lag to determine the phase shift caused by the Doppler Effect. The shift is calculated by the covariance method, which uses arctangent, therefore constraining the shift to a range of π to π [12]. In the instrument settings, this range is scaled to velocities based on the nominal flow velocity and specified range. If a value exceeds the range, phase wrapping occurs and the apparent measured shift is $\phi_{measured} = \phi_{actual} - 2\pi$. When this is mapped to the velocity it causes a large spike in the opposite direction of the measured value [12]. This is one reason for filtering ADV measurements with a despiking algorithm.

The Vectrino Profilers have one transmitter and four receiver heads. Recorded along-beam velocities calculated from the Doppler shift are transformed to instrument-frame velocities (u,v,z) by multiplying the receiver recorded beam magnitudes by a transformation matrix as show below.

$$\begin{bmatrix} T_{11} & T_{12} & T_{13} & T_{14} \\ T_{21} & T_{22} & T_{23} & T_{24} \\ T_{31} & T_{32} & T_{33} & T_{34} \\ T_{41} & T_{42} & T_{43} & T_{44} \end{bmatrix} \begin{bmatrix} b_1 \\ b_2 \\ b_3 \\ b_4 \end{bmatrix} = \begin{bmatrix} u_1 \\ u_2 \\ u_3 \\ u_4 \end{bmatrix} = \begin{bmatrix} u_x \\ u_y \\ u_{z1} \\ u_{z2} \end{bmatrix}$$

.

Since the Nortek Vectrino has four receivers the transformation matrix, T, has dimensions 4 x 4. The transformation matrix values are based on the geometry of the device. Since there are four receivers, there are four calculated velocities, meaning one of the Cartesian velocities will have two values [12]. Nortek has configured the Vectrino Profilers to record two velocities in the z axis.

2.2 Test Cases

2.2.1 Turbine

A straight bladed cross-flow turbine, 23.4 cm tall with a diameter of 17.2 cm, is used for all test cases in this study. The turbine has four identical NACA 0018 blades with a 4.06 cm chord length mounted equidistantly along the circumference of the swept area at a 7.1 degree positive pitch angle. The maximum Reynolds number of the blades at a flow rate of 0.7 m/s is approximately 7 x 10^{-4} (neglecting axial and angular induction)[11]. The straight bladed design was chosen for this study because of its relatively high efficiency of 19.4% compared to the helical bladed turbine, used by [9], of 18.1% in a flow of 1 m/s.

The turbine was mounted to a long shaft supported by top and bottom bearings (Figure 2.3) with the bottom bearing mounted to a suction plate. The turbine shaft was attached to torque cell, rotary encoder, and particle brake to characterize power performance [11].

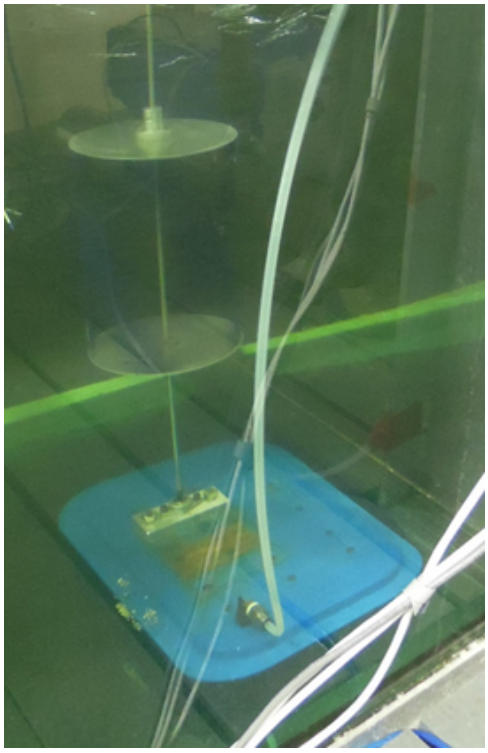

Figure 2.3: Turbine mounted with suction plate.

2.2.2 Measurement Grids

Transects 80 cm by 60 cm in the y-z plane at one, two, three, and five diameters downstream were measured with 5 cm grid resolution (Figure 2.4). Water velocity and turbine performance were measured for thirty seconds at each grid point, requiring slightly more than an hour.

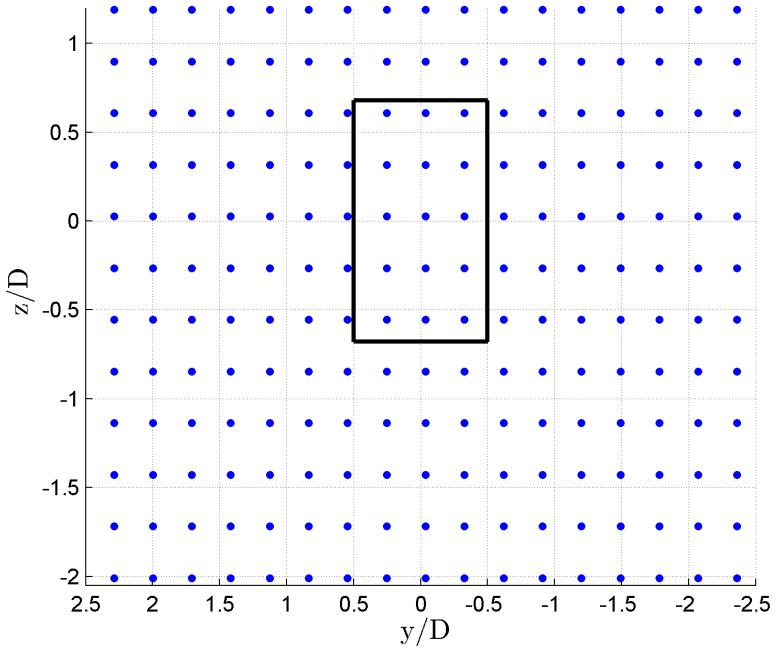

Figure 2.4: y-z plane measurement grid points. Rectangle represents turbine swept area.

Two denser grids, with 1 cm by 1 cm spacing, in the x-y plane were measured to better understand the near wake of the turbine. One grid covers the area 0.5 to 1.5 diameters in the y axis and 1 to 2 diameters downstream in the x-axis (Figure 2.5). The other grid was located symmetrically across the y-axis. Both grids were measured simultaneously with a pair of ADVs with a run duration just over three hours.

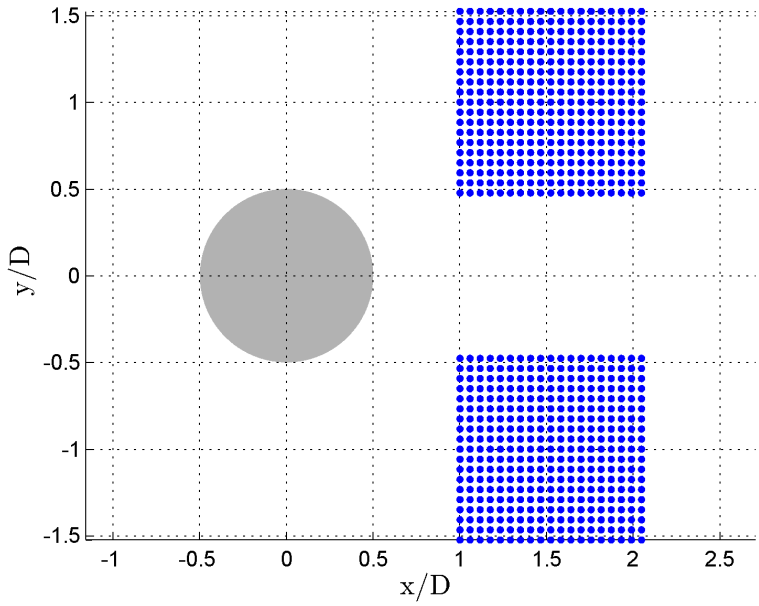

Figure 2.5: x-y plane measurement grid points. Circle represents turbine diameter.

2.3 Data Analysis

To quantify the wake structure mean velocity, turbulence intensity, coherent turbulent kinetic energy (CTKE), and Reynolds stresses were calculated from the measured velocity.

2.3.1 Measured Velocity

The velocity data from the ADVs contained non-physical spikes which were filtered out using a phase space de-spiking algorithm to identify outliers [8].

The mean velocity was computed for each velocity component at each grid point by averaging each velocity components over a thirty second measurement period. The instantaneous perturbation velocity for each component, denoted as u_i, is calculated by $u_i' = \overline{u} - u_i$. This represents the deviation of the velocity from the mean and is used to calculate CTKE and Reynolds stress.

2.3.2 Turbulence Intensity

Turbulence intensity, $I_u = \sigma_u/\overline{u}$, is a commonly used metric in the wind industry [7]. If calculated for an individual velocity, for example, the u component, as $I_u = \sigma_u/\overline{u}$. This represents the amount of velocity variation in one direction of the flow and can be calculated in all three dimensions (I_u, I_v, I_w). Another method is to calculate the velocity magnitude and then calculate a non-directional turbulence intensity magnitude as, $I_U = \sigma_U/\overline{U}$. Each method can provide different information of the turbulence present in a flow.

2.3.3 Reynolds Stress

Reynolds stress is defined as density times the stress tensor of a fluid, $\rho(\overline{u_i' u_j'})$, with the normal stresses ($\overline{u'^2}$,$\overline{v'^2}$,$\overline{w'^2}$) on the diagonal and shear stresses ($\overline{u'v'}$,$\overline{u'w'}$,$\overline{v'w'}$,etc.) populating the off diagonal components.

$$\rho(\overline{u_i' u_j'}) = \rho \begin{pmatrix} \overline{u'u'} & \overline{u'v'} & \overline{u'w'} \\ \overline{v'u'} & \overline{v'v'} & \overline{v'w'} \\ \overline{w'u'} & \overline{w'v'} & \overline{w'w'} \end{pmatrix}$$

.

The Reynolds stress can be used to identify the primary stresses in a fluid.

2.3.4 Coherent Turbulent Kinetic Energy

Coherent turbulent kinetic energy is an instantaneous quantity calculated from shear stresses and is defined as, $1/2\sqrt{(u'w')^2 + (u'v')^2 + (v'w')^2}$. CTKE is used to identify spatially coherent structures on the basis of elevated shear stress [7].

2.3.5 Phase-Locked Analysis

The wake was analyzed in two ways: the first by averaging parameters temporally for each grid point, and the second by locking the velocity data to the turbine encoder position, which is referred to as "phase-locked", encoder position does not correspond to an absolute

turbine blade position, so it is difficult to draw specific conclusions about the origin of coherent structures identified in the phase-locked analysis. The encoder outputs 500 pulses per revolution and the turbine rotates approximately 10 radians per second. However, the velocity data is only being sampled at 100 Hz, meaning the smallest resolvable arc segment is 3 degrees. Phase-locked parameters are averaged by the encoder position into 18 degrees bins to provide a sufficient number of points for statistical analysis. This results in 20 bins over a complete rotation.

Chapter 3

RESULTS

Results for velocity, turbulence intensity, coherent turbulent kinetic energy, and Reynolds shear stress are presented as averages over the 30 second measurement period. Phase-locked CTKE and Reynolds stresses are also presented to analyze changes in the wake as a function of turbine angular position.

3.1 Velocity

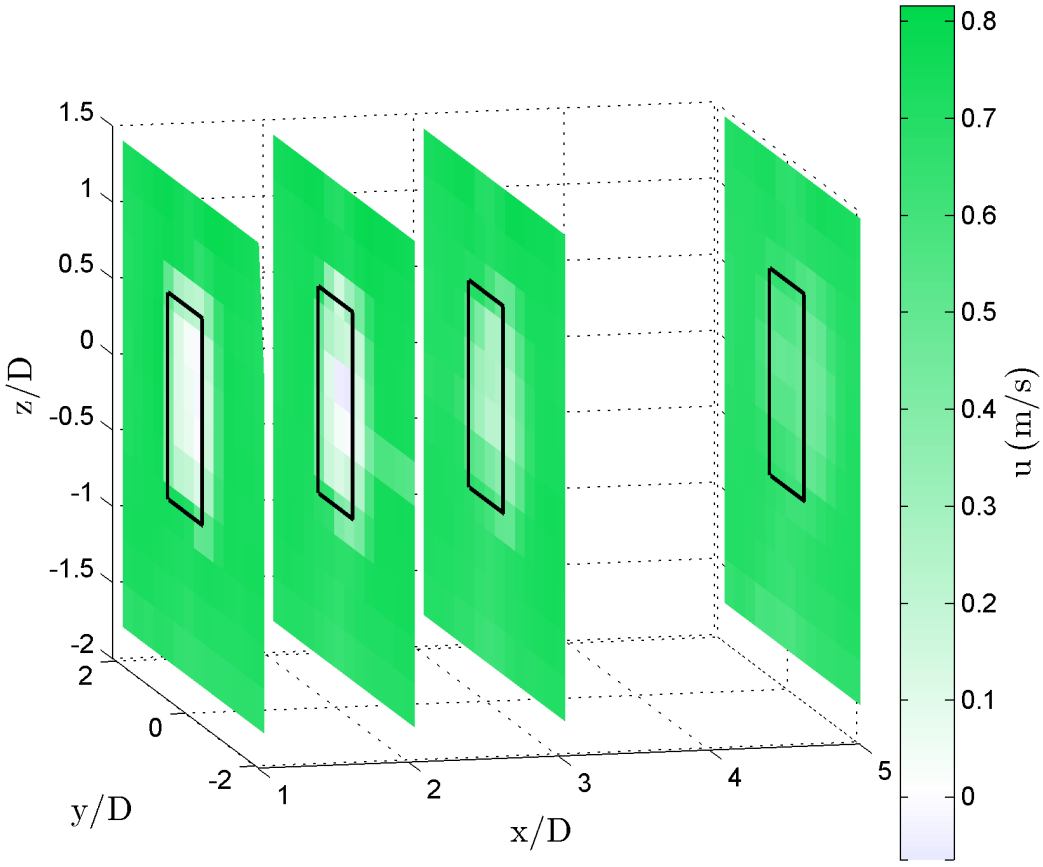

Figure 3.1: u at 1,2,3, and 5 diameter downstream transects.

At one diameter behind the turbine, the area of the turbine wake is apparent by the low u-velocity shown in the y-z planes (Figure 3.1). The bypass flow has a velocity of 0.72 m/s, but the flow behind the turbine cross-section has been reduced to 0.1 m/s or lower. Moving downstream, the velocity deficit decreases, but shows a clear asymmetry in the negative y-direction. This is also shown by Figure 3.2, in the x-y plane.

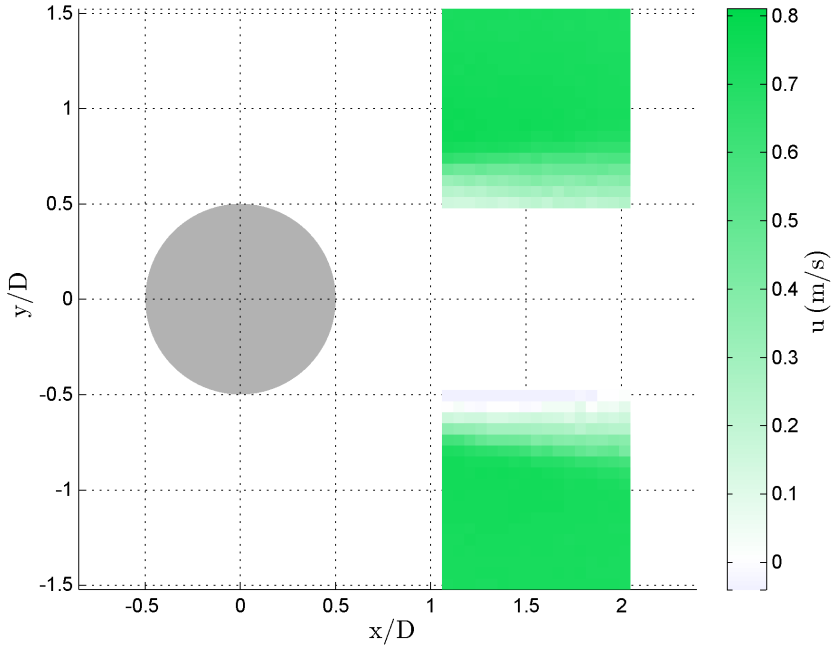

Figure 3.2: u in the x-y plane between 1 and 2 diameters downstream.

The v velocity shows a small negative bias for all y-z planes (Figure 3.3). This is a consequence of an incorrectly specified coordinate transformation matrix identified over the course of these experiments. [a]

[a]The recorded v velocity is almost entirely negative, shown by Figure 10. This flow cannot be physically supported in a flume because of the walls. After contacting Nortek AS, it was discovered that both of the Vectrino Profilers may have incorrect coordinate transformations, resulting in a v velocity bias. In addition, one of the Vectrinos has a damaged receiver head. This is identified by a low beam amplitude when performing a probe check on the instrument. The instruments have been sent back to Nortek AS, who received the devices on November 23, 2014, for recalibration and repair. This paper focuses on relative differences instead of quantitative results because of the miscalibration of the instruments.

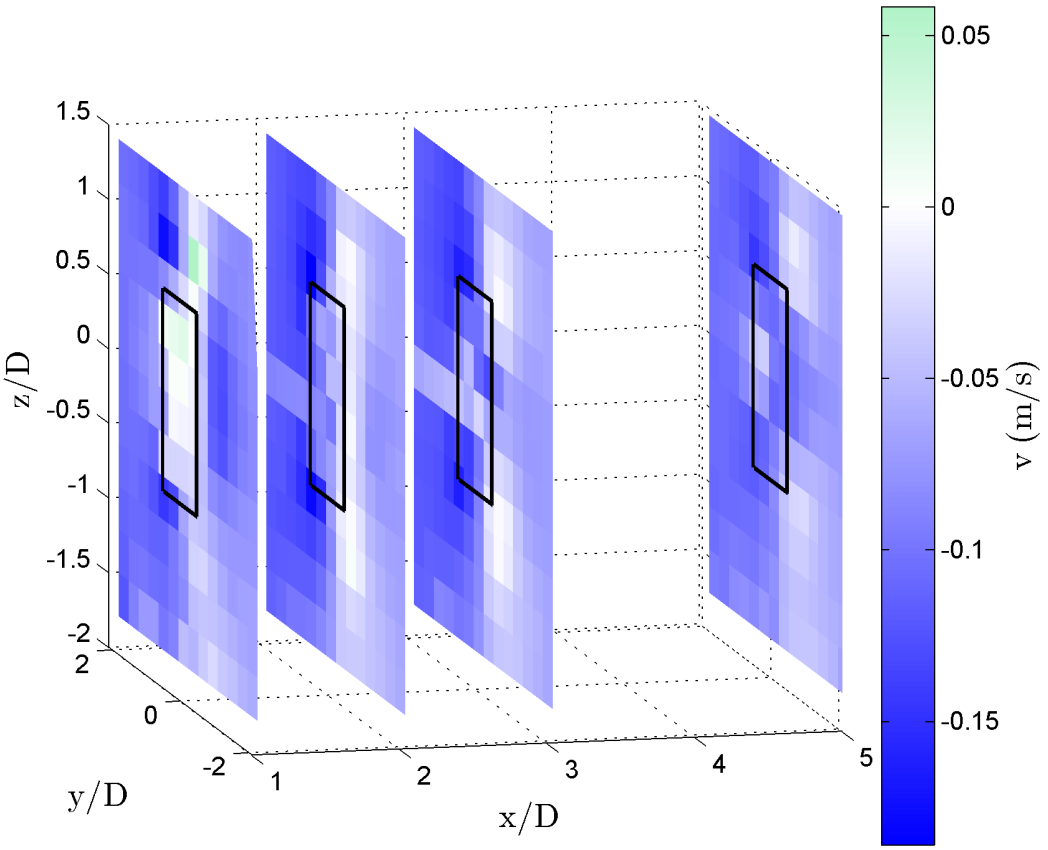

Figure 3.3: v-velocity at 1,2,3, and 5 diameter downstream transects.

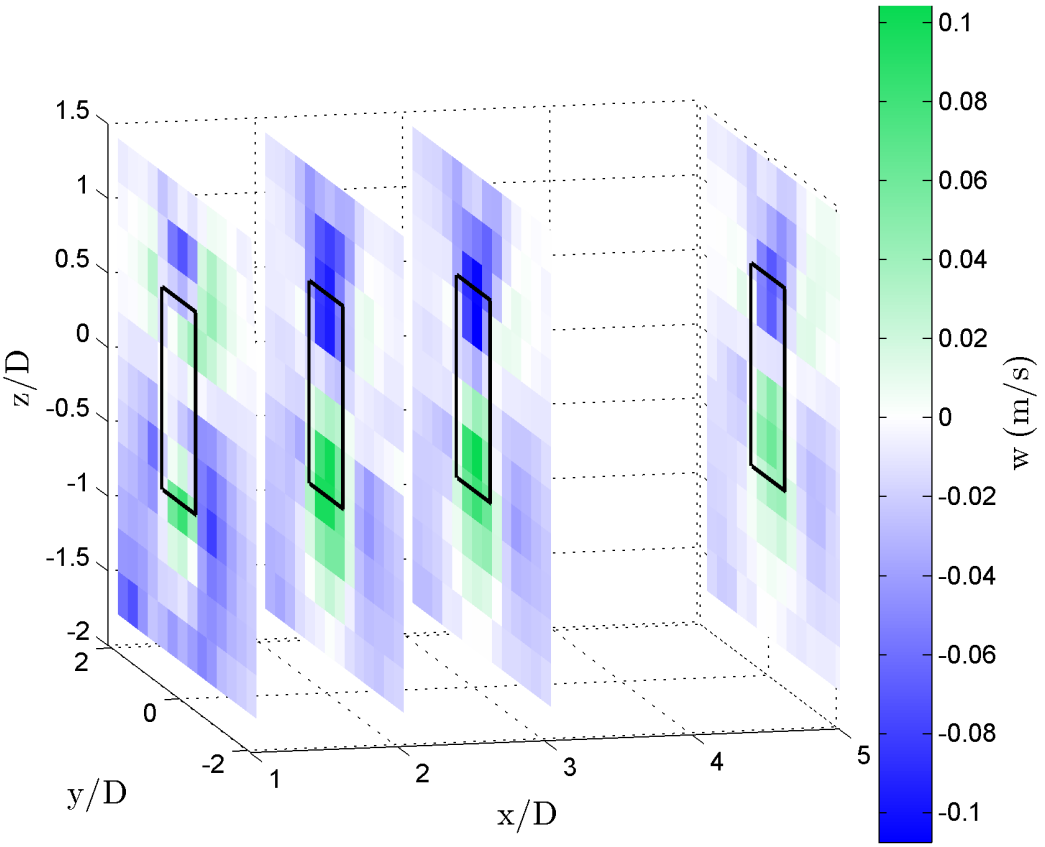

Figure 3.4: w-velocity at 1,2,3, and 5 diameter downstream transects.

There are two regions of relatively large w velocity (one positive and one negative), as shown in transects 2, 3, and 5 diameters downstream in Figure 3.4, compared to the rest of the flow. One region is at the bottom of the turbine cross-section with a positive w-velocity and the other region is located at the top of the turbine cross-section with a negative w velocity. These regions are more persistent than the u and v velocity wake.

The w-velocity in the x-y plane (Figure 3.2) shows two regions of negative velocity located in the turbine wake. Some points of positive velocity are found on the negative y side of the turbine, which contrast the completely negative sign region on the positive y side of the turbine. It is possible that a similar positive region is not observed on the positive y side of the turbine as a consequence of the portion of the asymmetric wake that was sampled.

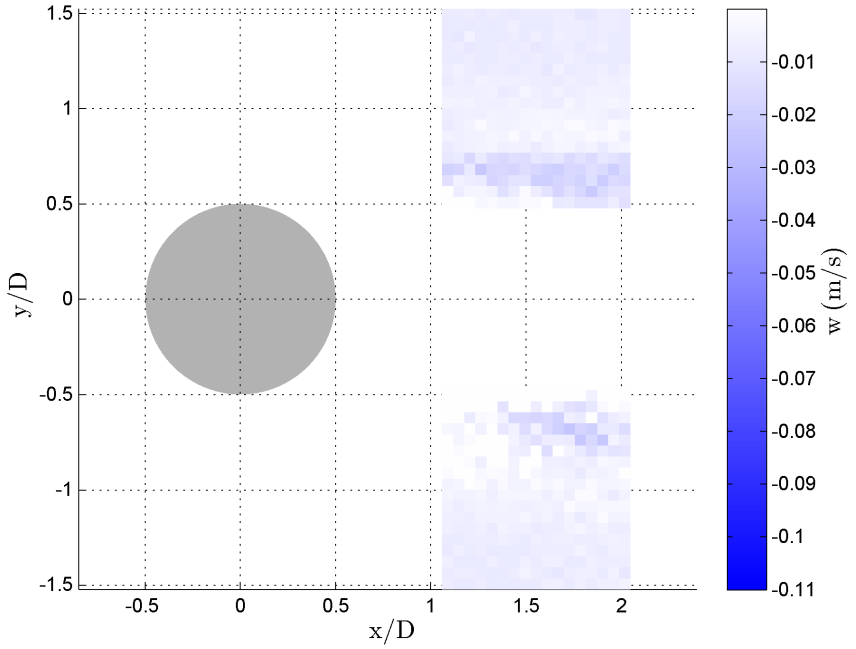

Figure 3.5: w-velocity in the x-y plane between 1 and 2 diameters downstream.

3.2 Turbulence Intensity

The stream-wise turbulence intensity, I_u, peaks at two diameters and then decreases to nearly zero moving at five diameters (Figure 3.6).

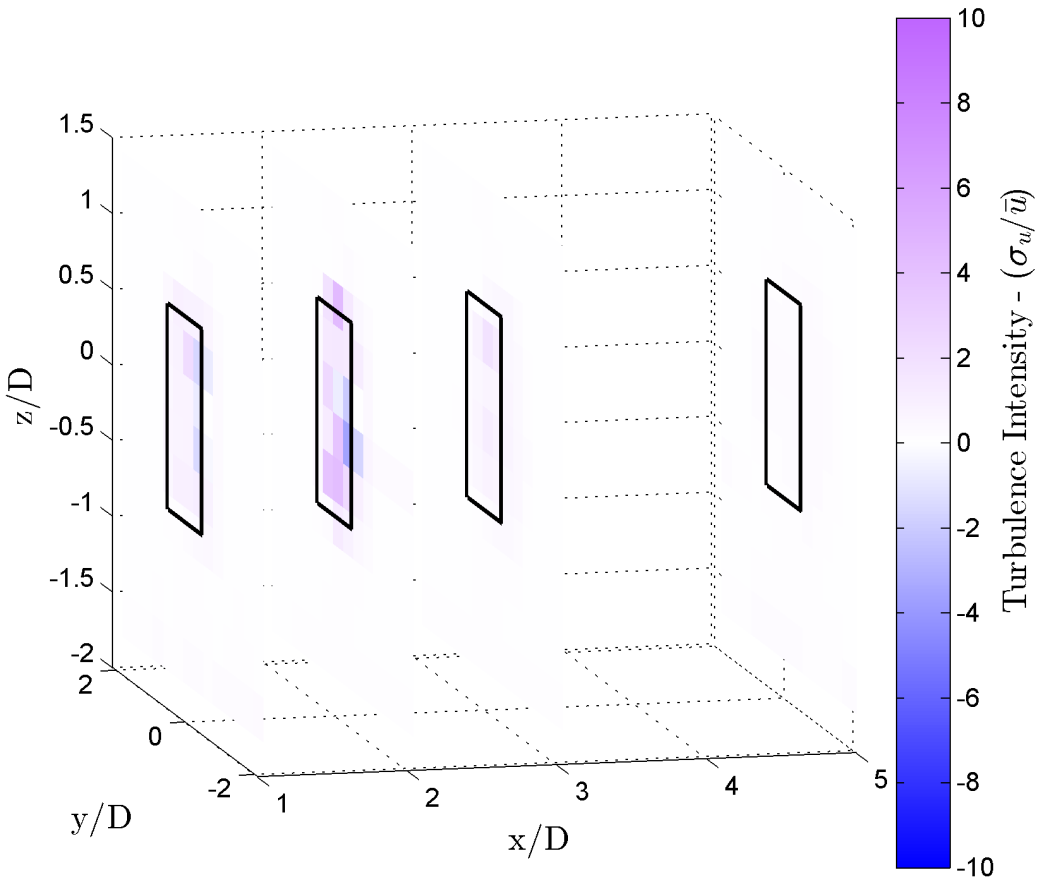

Figure 3.6: Turbulence intensity, u-velocity, at 1,2,3 and 5 diameter transects downstream.

The turbulence intensity is much higher in the y and z directions as a result of strong perturbations with low mean velocities.

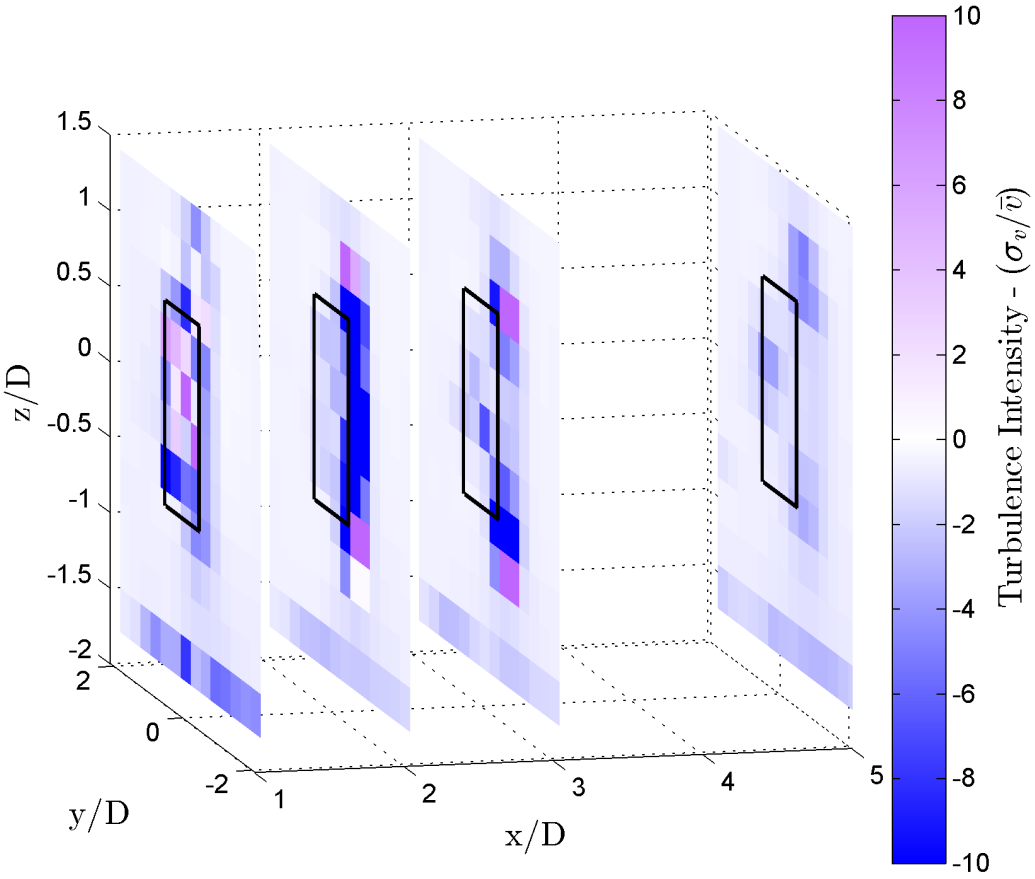

Figure 3.7: Turbulence intensity, v-direction (saturates at $I_v = 10$).

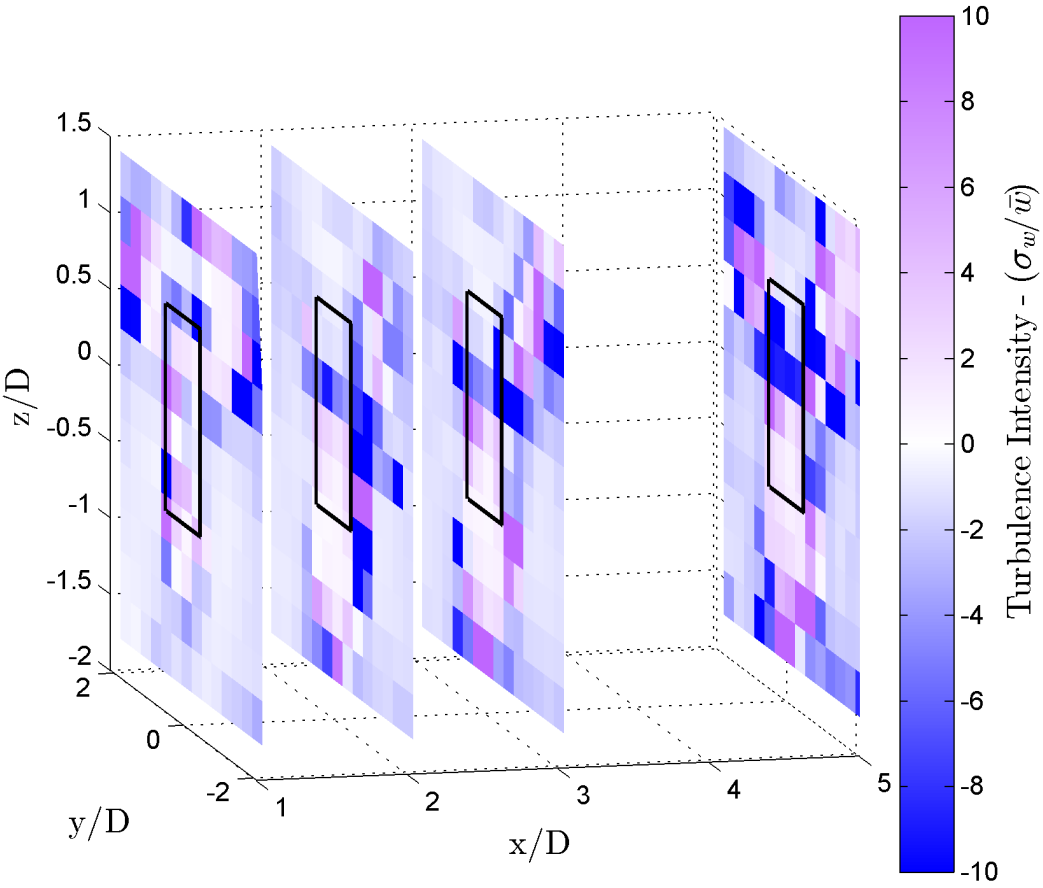

Figure 3.8: Turbulence intensity, w-direction (saturates at $I_w = 10$).

The turbulence intensity in the vertical direction does not display any meaningful structure for most of the transects. At one diameter most of the turbulence is located in the positive z quadrants but the other transects appear more random. Comparatively, the cross-stream turbulence is mostly confined to the turbine cross-sectional area. Just as with I_u, the peak turbulence is at two diameters but is biased to the negative y side of the turbine. Turbulence intensity magnitude I_U (Figure 3.9), provides a better visual of the overall wake structure than breaking into velocity components. These values of turbulence intensity are also in closer agreement with prior results (e.g., Bachant and Wosnik 2013).

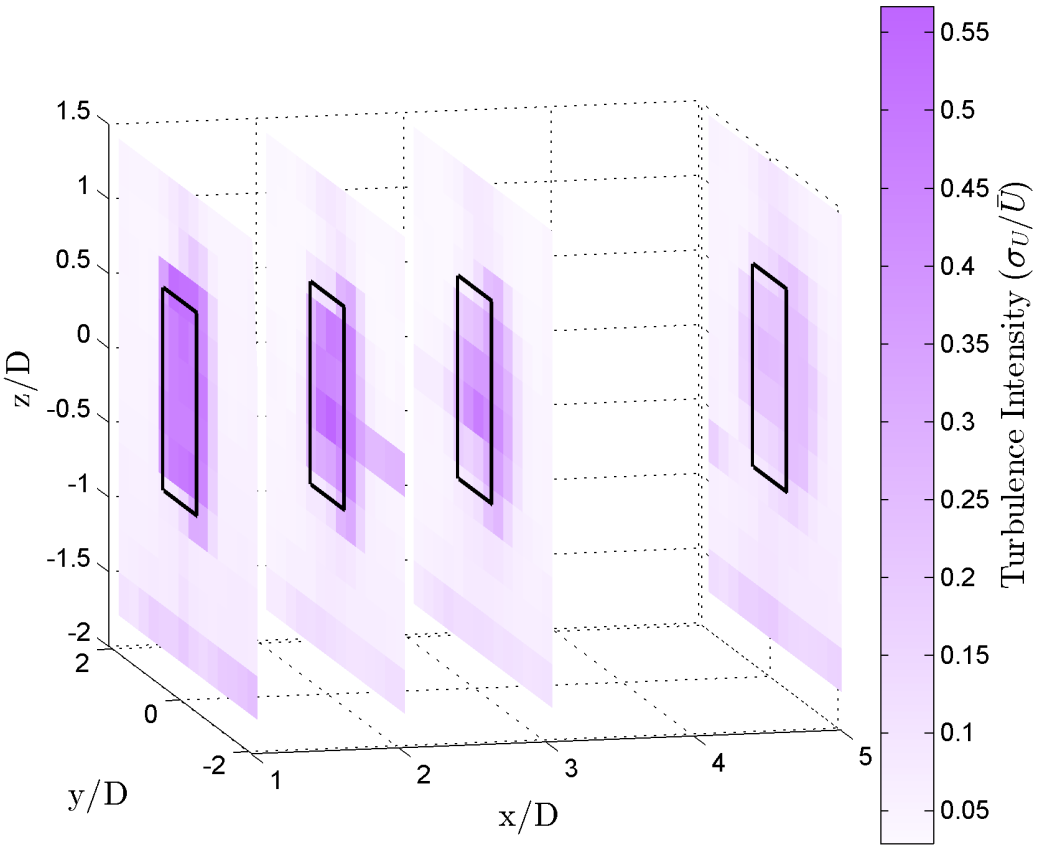

Figure 3.9: Turbulence intensity of velocity magnitude.

Other than the shear layer at the bottom of the flume, the turbulence intensity is confined to the turbine wake. A maximum is seen in the one diameter transect, decreasing in size and magnitude with downstream position.

3.3 Coherent Turbulent Kinetic Energy

At one diameter downstream, the highest CTKE values form a rectangular ring corresponding to the edge of the turbine swept area (Figure 3.10). This is consistent with coherent vortices shed by the turbine blades, which diffuse at downstream positions.

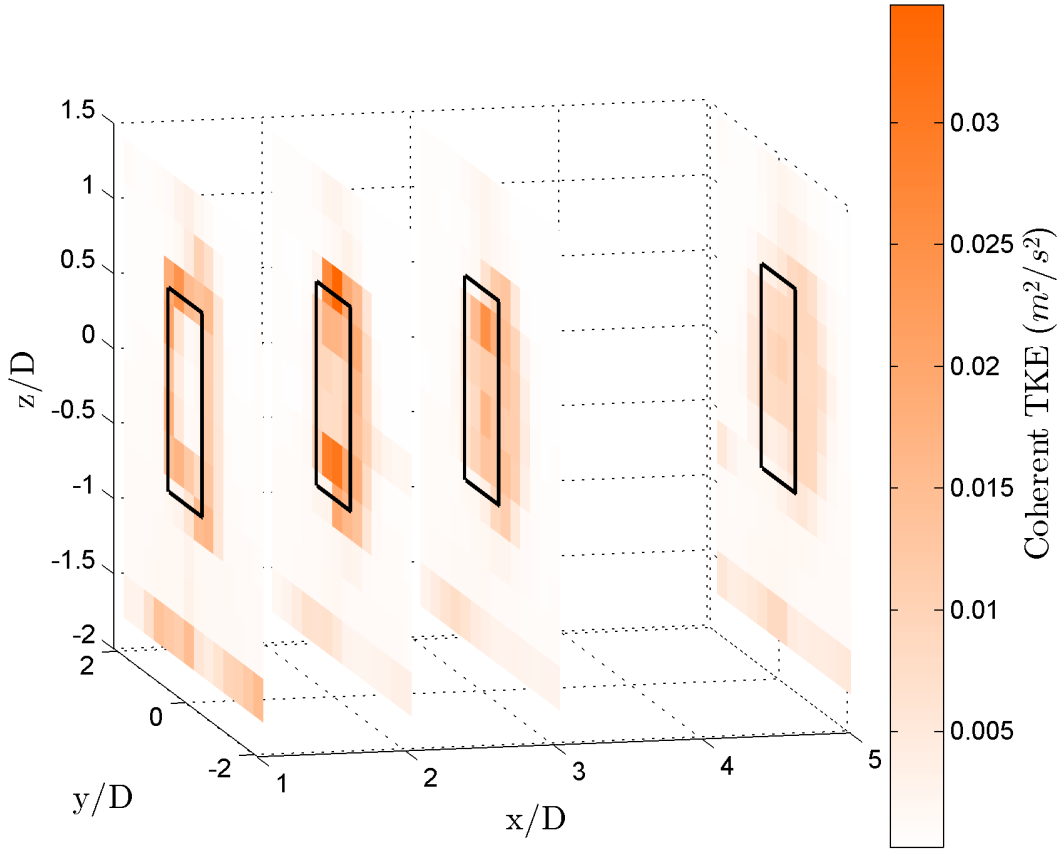

Figure 3.10: Coherent turbulent kinetic energy at 1, 2, 3, and 5 diameter downstream transects.

The shear layer in the wake appears to be expanding, with a V-shape clear on the negative y side of turbine (Figure 3.11).

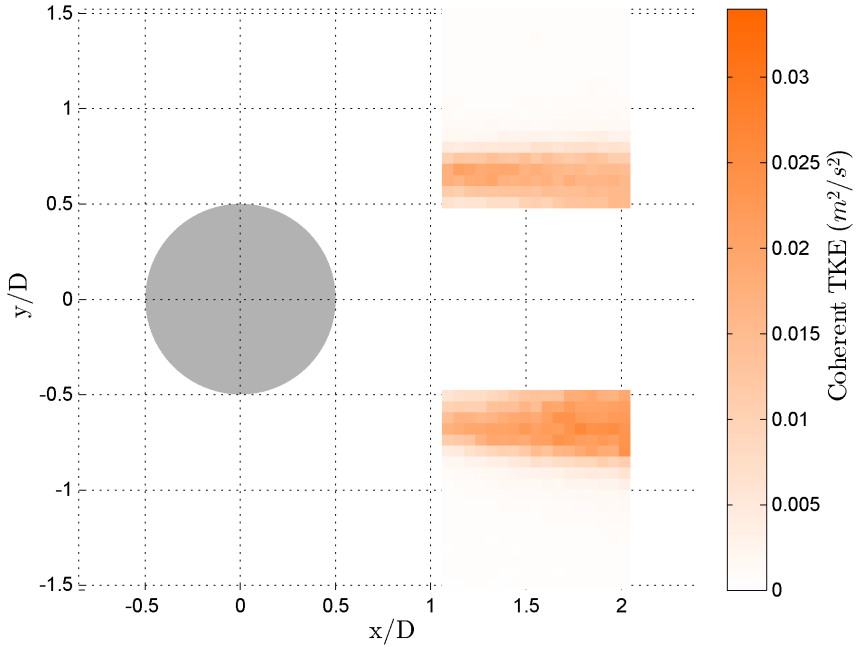

Figure 3.11: Coherent turbulent kinetic energy x-y plane between 1 and 2 diameters downstream.

3.4 Reynolds Stress

The Reynolds shear stresses in the x-y plane show the evolution of the shear layer separating the wake from the free stream(Figure 3.12). The shear is highest predominantly in the $u'v'$ component (order of magnitude larger than in the $u'w'$ and $v'w'$ components).

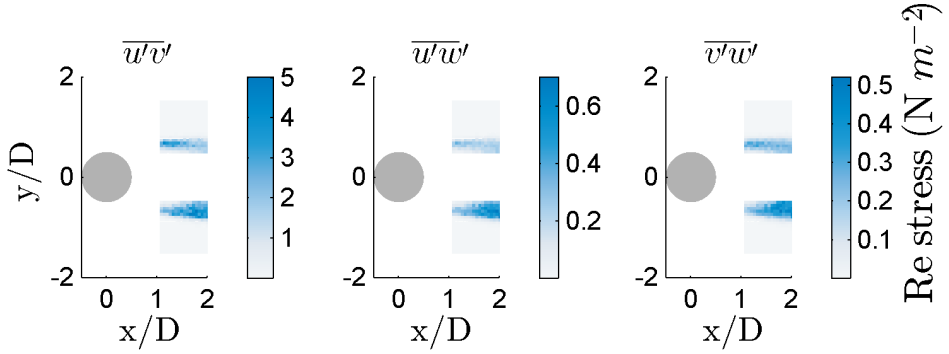

Figure 3.12: Reynolds shear stress in the x-y plane.

Just as with CTKE, the rectangular ring of the shear layer is evident at one diameter in all of the shear components (Figures 3.13,A.3,& A.4). At two diameters the $\overline{u'v'}$ and $\overline{u'w'}$ shear are confined to two regions at the top and bottom of the turbine swept area and separated by a region of low magnitude. The $\overline{v'w'}$ shear does not share this shape, but is more of an oval located on the negative y side of the turbine. The two $\overline{u'v'}$ and $\overline{u'w'}$ regions become less distinguishable further downstream.

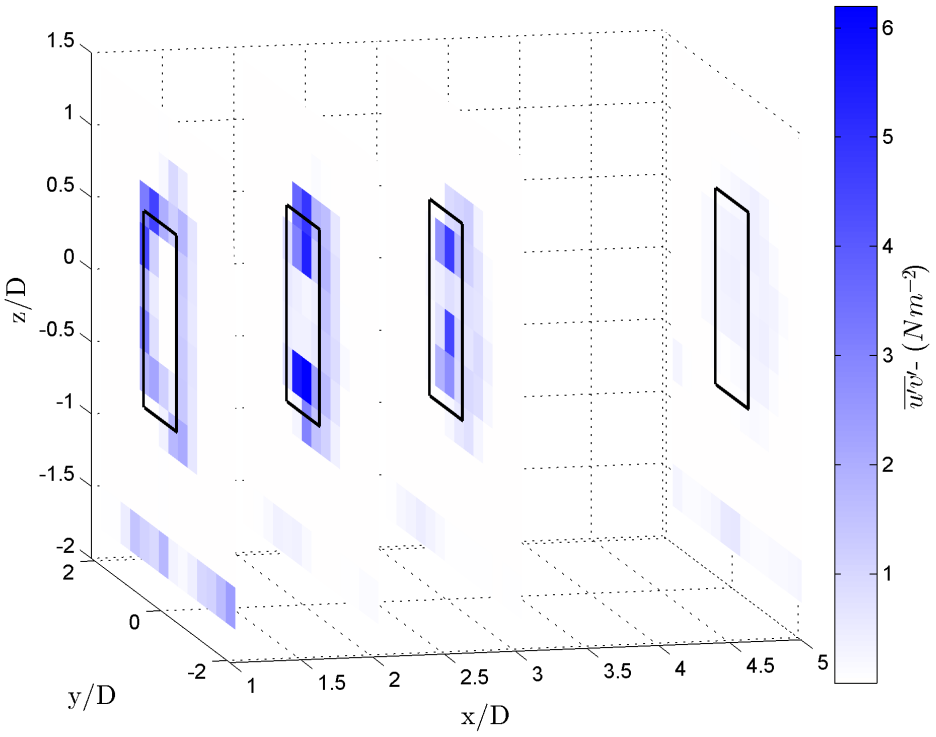

Figure 3.13: $\overline{u'v'}$ Reynolds stress in the y-z plane.

3.5 Phase-Locked CTKE

For all transects, some of the phase-locked CTKE bins match the profiles of the time series averaged CTKE. At one diameter downstream, the phase-locked CTKE (Figure A.5), matches the rectangular ring profile of the full time series averaged CTKE for roughly half of the angular bins. The remainder have turbulence in the positive-y upper swept turbine

area, but are confined to the wake. Moving downstream, the phase locked bins match the phase-averaged transects, where the wake begins to mix and the CTKE profile changes from a rectangular ring into a less defined oval (Figures A.6, A.7, A.8), as would be expected to occur as the coherent vortices break up in the wake shear layer.

At all distances downstream there is clearly some periodic nature to the CTKE magnitude and structure. This is easily seen at five diameters, Figure A.8, where there are two regions of relatively high magnitude CTKE. The first region spans bins 0 - 72°and the second region bins 217 - 270°. After each of these regions there are bins, 91 - 126°, and 289 - 324°, with significantly less coherent turbulence. Moving towards the turbine, the frequency of high magnitude regions increases. At three diameters, Figure A.7, there are three regions: 325 - 18°, 127 - 198°, and 235 - 288°. There is a large gap between region 325 - 18°and 127 - 198°, whereas the gap between the other regions is much smaller.

It is a more difficult to identify high-activity regions in the one and two diameter transects. In an attempt to find a pattern, there are four potential regions at two diameters: 325 - 36°, 73 - 108°, 163 - 180°, and 235 - 306°(Figure A.6). The regions from 73 - 108°and 163 - 180°could be grouped together to form one larger region resulting in three total peaks.

At one diameter, Figure A.5, identifiable regions are even less clear, but there seem to be bursts of activity along the positive x-axis side of the turbine cross-section and the positive x and y axes upper corner of the turbine cross-section.

3.6 Phase-Locked Reynold's Shear Stresses

The high magnitude points in CTKE correspond to high Reynolds shear stresses in the same bins, which is expected since the shear stresses are used to calculate CTKE (Figure 3.14).

Re Stress	**Transect**			
	1D	2D	3D	5D
$\overline{u'v'}$	11	3.25	0.85	3.2
$\overline{v'w'}$	0.26	1.4	0.62	1.4
$\overline{u'w'}$	0.085	1.45	0.26	1.5

Table 3.1: Reynolds shear stress maximum magnitude by transect.

Even though, the $\overline{u'v'}$ stress has the highest magnitude it does not make up the all of the CTKE. The first bin, 0-18°, at two diameters downstream is an example of this. All three shear components of stress contribute to the CTKE. While the $\overline{u'v'}$ component is the largest, some of the shear on the negative y side of the turbine cross-section comes from the $\overline{u'w'}$ and $\overline{v'w'}$ shear components.

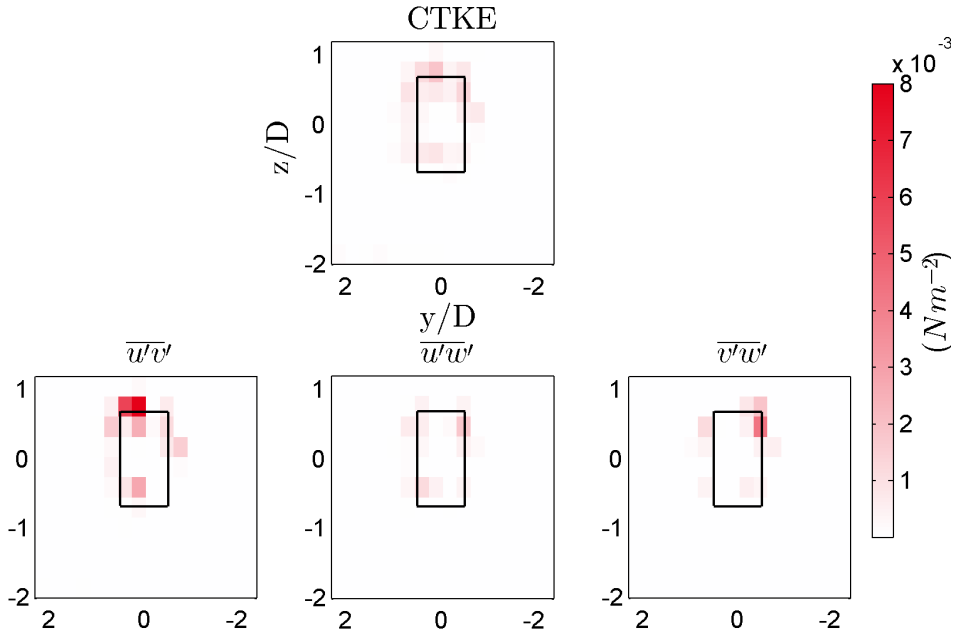

Figure 3.14: Reynolds shear stress and CTKE in phase-locked bin 0-18°at 2 diameters.

Chapter 4
DISCUSSION

4.1 Velocity

The turbine wake is clearly defined at one diameter, shown by the u velocity transect (Figure 3.1), as a rectangle matching the turbine cross-section profile. Moving downstream the wake begins to mix with the surrounding flow and recovers some velocity in the x-direction. At five diameters downstream, the wake has not fully mixed but no longer has such a defined boundary with the bypass flow compared to the one, two, and three diameter transects.

There is a clear bias to the wake from the rotation of the turbine. If the wake is split into two parts, positive y and negative y sides divided by the y-axis, Figure 3.2 shows that the wake is wider on the negative y side by the larger light green region. Figure 3.2 also shows that the wake expands outwards between one and two diameters downstream. However, in the distance between two and three diameters the apparent wake begins to contract, shown by Figure 3.1, as it mixes with the bypass flow.

The larger magnitude w velocity regions, in Figure 3.4, propagate far downstream so it is unlikely that these are from shed tip or leading edge vortices. More likely, this is fluid from the bypass flow mixing with the wake. As fluid moves around an object, it first expands and then contracts to mix with the deficit region. In the case of the turbine, fluid passing below the turbine is moving upwards and fluid passing above the turbine is moving downwards as the wake mixes with the bypass flow.

w-velocity in the near wake (Figure 3.5) is larger than the bypass surrounding flow. This is most likely from mixing with the bypass flow but could also be associated with vortices shed by the turbine blades (i.e. a vortex in the x-y plane will transport fluid in the z direction).

4.2 Turbulence Intensity

The turbulence intensity magnitude (Figure 3.9), matches the u velocity deficit (Figure 3.1) and confirms that turbulence is greatest inside the wake. As expected, the highest intensity and largest extent is located closest to the turbine and decreases in the downstream direction. The component turbulence intensities have large magnitudes and do not match the magnitude profile well. This suggests that the turbulence intensity of the velocity magnitude may be a better metric to describe the wake structure.

4.3 Coherent Turbulent Kinetic Energy

The rectangular ring at one diameter (Figure 3.10) suggests that the CTKE is confined to the shear layer between the bypass flow and the turbine wake. At one diameter, there is still a large velocity gradient between the turbine wake and bypass flow, which was clear from the u velocity transect plot (Figure 3.1). The shear layer grows in the y-z plane as one moves downstream.

4.4 Reynolds Stress

The V shape confirms that the shear layer is expanding in the downstream direction, consistent with fluid kinematics. Although transect results are only shown in the y-z plane (Figure 3.12), the V shape can be extrapolated to three dimensions to explain the CTKE rectangular ring evident in Figure 3.10. For the x-y plane (Figure 3.12), a higher magnitude is expected for the $u'v'$ shear because flume flow is primarily in the x-direction. The u-velocity difference between the bypass flow and fluid in the turbine wake will produce a shear layer with mixing vortices in the x-y plane, thus the $u'v'$ shear. The shear layer in the wake is apparent in the Reynolds stress measurement (Figure 3.12) and is consistent with the shape of the peak CTKE in the y-z plane. The two $u'v'$ and $u'w'$ regions at two diameters may be coherent structures and may be responsible for the colocated higher magnitude w velocity regions (Figure **??**). Vortical structures will transport fluid in the direction of their rotational axis.

4.5 Phase-Locked CTKE

For one full turbine rotation, four bursts of CTKE would be expected to match the number of blades. However, at five diameters, there are only three burst of identifiable CTKE. The four bursts at two diameters may represent turbulent structures shed by the blades. The decreasing frequency in bursts may be vortices rolling up into larger, more diffuse, vortexes, which is consistent with the unequal spacing found at five diameters (Figure A.8). Bursts may not be apparent at one diameter because bins of 18 degrees may not be small enough to resolve smaller, more intense, turbulent structures near the turbine.

4.6 Phase-Locked Reynold's Shear Stresses

In general, the $u'v'$ shear stress has a higher magnitude than the other shear components. The $u'v'$ term could represent leading or trailing edge vortices based on the geometry of the turbine (i.e., blade rotation is in the x-y plane). Although it is not clear how the tip vortex interacts with the turbine endplates, we expect shed tip vortices to be represented by the $v'w'$ and $u'w'$ components because of the turbine geometry (i.e, blades are mounted vertically and vortices will interact with horizontal velocity components).

Chapter 5
CONCLUSION

The results of this study are consistent with previous experimental and modeling work. Just as in Bachant and Wosnik (2013), the wake was found to be asymmetrical, which may be relevant when spacing turbines close to each other or objects. In terms of wake propagation, this study found at five diameters, the wake stream-wise velocity at the center of the wake, about 70% of the free stream, is fairly close to Niblick 2012 findings of 60% for a sparse grid with a helical turbine.

The vorticity simulation by Scheurich et al. 2011 used a finer mesh than any of the measurement grids in this study. In the present study, the relatively large grid spacing makes it hard to identify vortical structures and find similarities in the results of both studies. However, bursts of CTKE in the phase-locked figures show that periodic coherent structures are present.

Component velocity gives an initial visualization of the turbine wake as a rectangular stream-wise deficit that mixes with the bypass flow. This shape is also evident in the magnitude turbulence intensity. However, neither of these representations provide information about the shear layer. Coherent turbulent kinetic energy and Reynolds shear stresses can identify the shear layer, mixing in the wake, and potential vortical structures. A finer resolution grid and higher velocity sampling rates can improve the analysis of the shear layer and coherent structures, albeit with greater time investment.

The implementation of an automated gantry with ADVs to measure water velocity proves to be a useful method to characterize turbine wakes. Future work can use the results of this study to identify locations in the wake of coherent structures and particle image velocimetry could be used to obtain synoptic characterization of the wake. These methods can be

combined to understand the factors that influence individual turbine performance and the operation of turbines in dense arrays.

BIBLIOGRAPHY

[1] Bislide engineering specifications. http://www.velmex.com/bislide/motor_bislide_spec.html.

[2] Untitled image of verdant power turbine, 2014. http://www.verdantpower.com/media-gallery.html.

[3] C. L. Archer, S. Mizaeisefat, and S. Lee. Quantifying the sensitivity of wind farm performance to array layout options using large-eddy simulation. *Geophys. Res. Lett.*, 40(49634970), 2013.

[4] P. Bachant and M. Wosnik. Performance of near-wake measurements for a vertical axis turbine at moderate reynolds number. ASME Fluids Engineering Summer Meeting, July 2013.

[5] R. Cavagnaro and B. Polagye. An evaluation of blockage corrections for helical cross-flow turbine. 3rd Oxford Tidal Energy Workshop, April 2014. http://www.eng.ox.ac.uk/tidal/ote-papers/2014/p07.

[6] Y. Li and S. M. Calisal. Modeling of twin-turbine systems with vertical axis tidal current turbines: Part I-power output. *Ocean Engineering*, 37:627–637, 2010.

[7] K. McCaffery, B. Fox-Kemper, P.E. Hamilton, and J. Thomson. Characterization of turbulence anisotropy, coherence, and intermittency at a prospective tidal energy site: Observational data analysis. *Accepted to Renewable Energy*, 2014.

[8] N. Mori, T. Suzuki, and S. Kakuno. Noise of acoustic doppler velocimeter data in bubbly flow. *Journal of Engineering Mechanics, American Society of Civel Engineers*, 133(1):122–125, 2007.

[9] Adam Niblick. Experimental and analytical study of helical cross-flow turbines for a tidal micropower generation system. Master's thesis, University of Washington, 2012.

[10] B. Polagye, R. Cavagnaro, A. Niblick, T. Hall, J. Thomson, and A. Aliseda. Cross-flow turbine performance and wake characterization. Marine Energy Technology Symposium, 2013.

[11] B. L. Polagye, R. J. Cavagnaro, and A. L. Niblick. Micropower from tidal turbines. ASME 2013 Fluid Engineering Division Summer Meeting, July 2013.

[12] Peter J. Rusello. A practical primer for pulse coherent instruments. Technical report, Nortek AS, 2009. `http://www.nortekusa.com/lib/technical-notes/tn-027-pulse-coherent-primer`.

[13] F. Scheurich, T. M. Fletcher, and R. Brown. Simulating the aerodynamic performance and wake dynamics of a vertical-axis wind turbine. *Wind Energy*, 14(2):159–177, 2011.

[14] DC Central Intelligence Agency. Washington. The World Factbook 2013-14, 2013.

Appendix A

APPENDIX

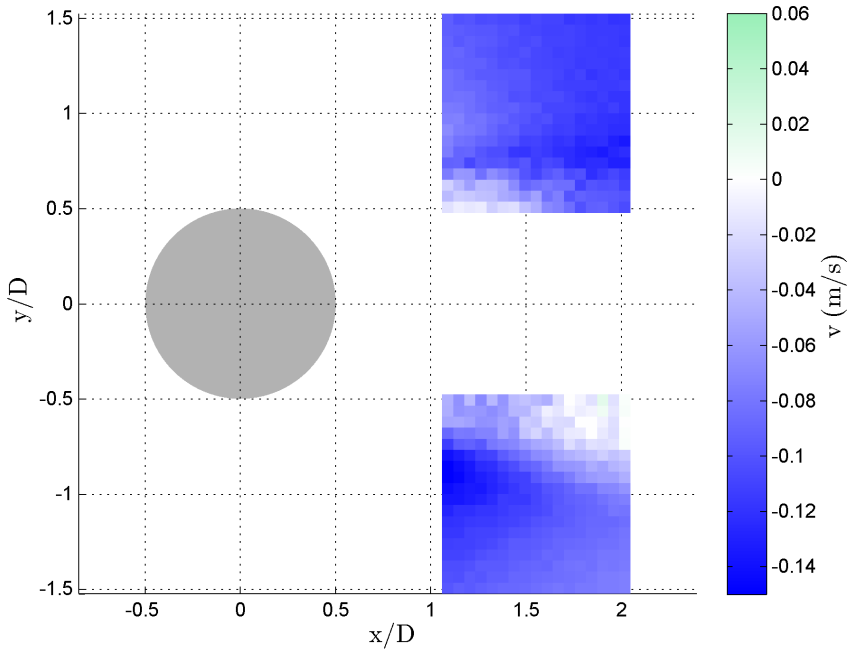

Figure A.1: v-velocity in the x-y plane between 1 and 2 diameters downstream.

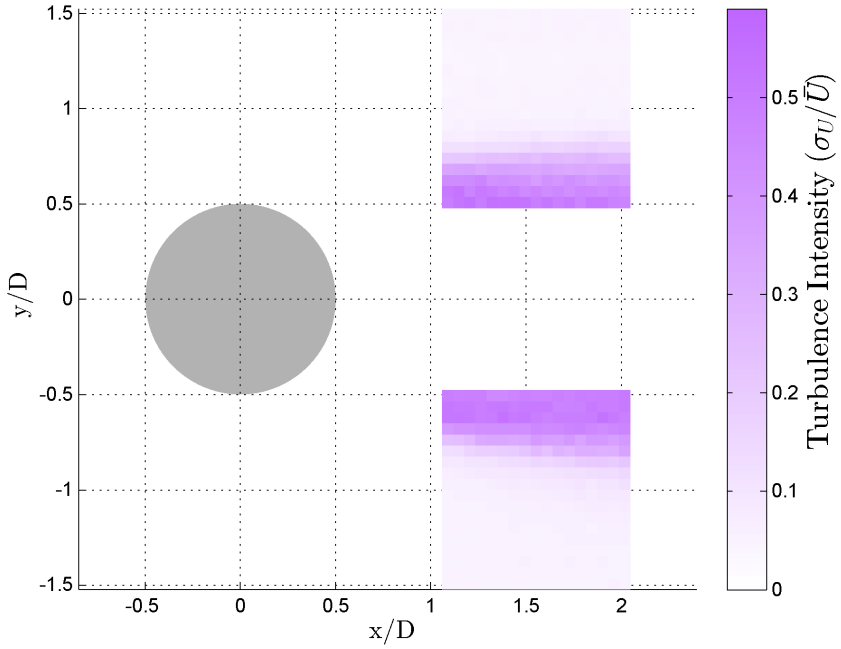

Figure A.2: Turbulence intensity in the x-y plane between 1 and 2 diameters downstream.

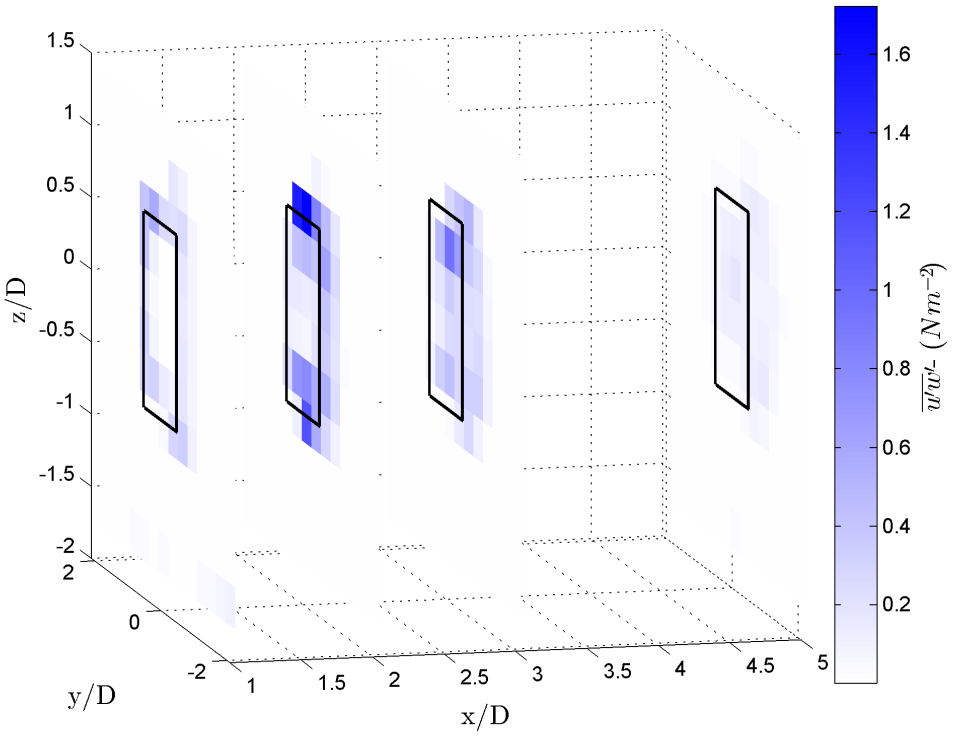

Figure A.3: $\overline{u'w'}$ Reynolds stress in the y-z plane.

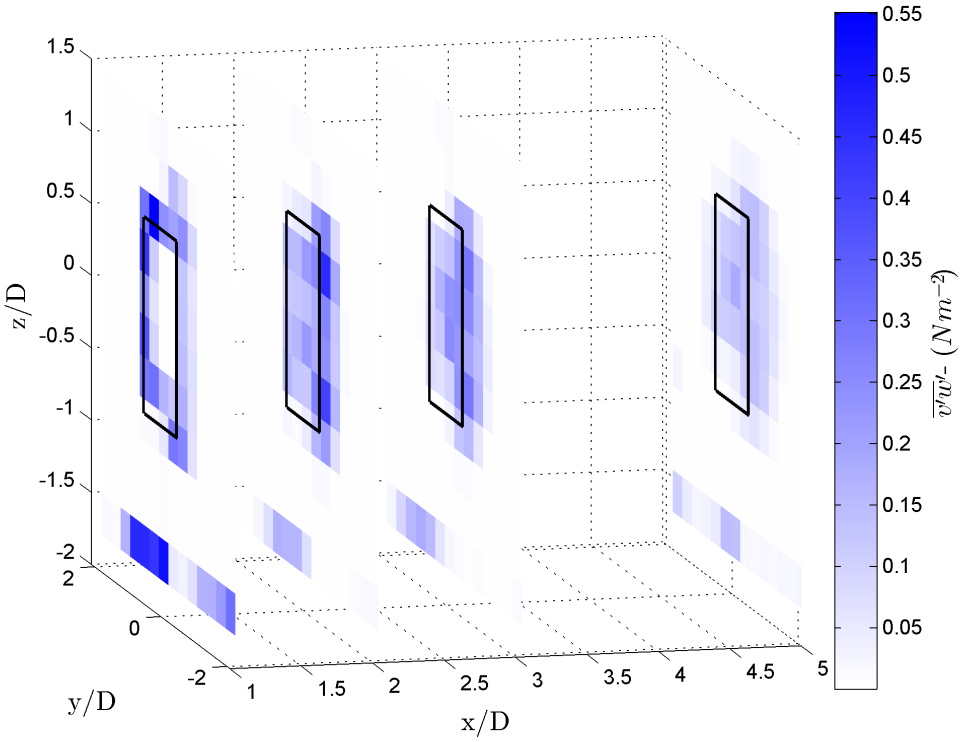

Figure A.4: $\overline{v'w'}$ Reynolds stress in the y-z plane.

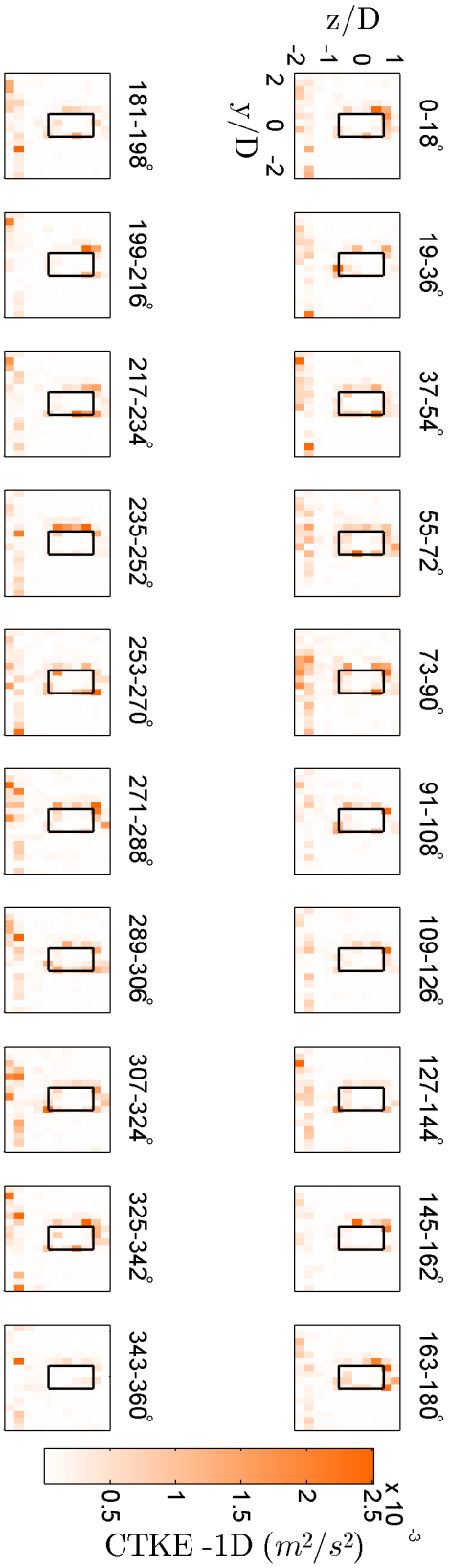

Figure A.5: Phase-locked CTKE at 1 diameter.

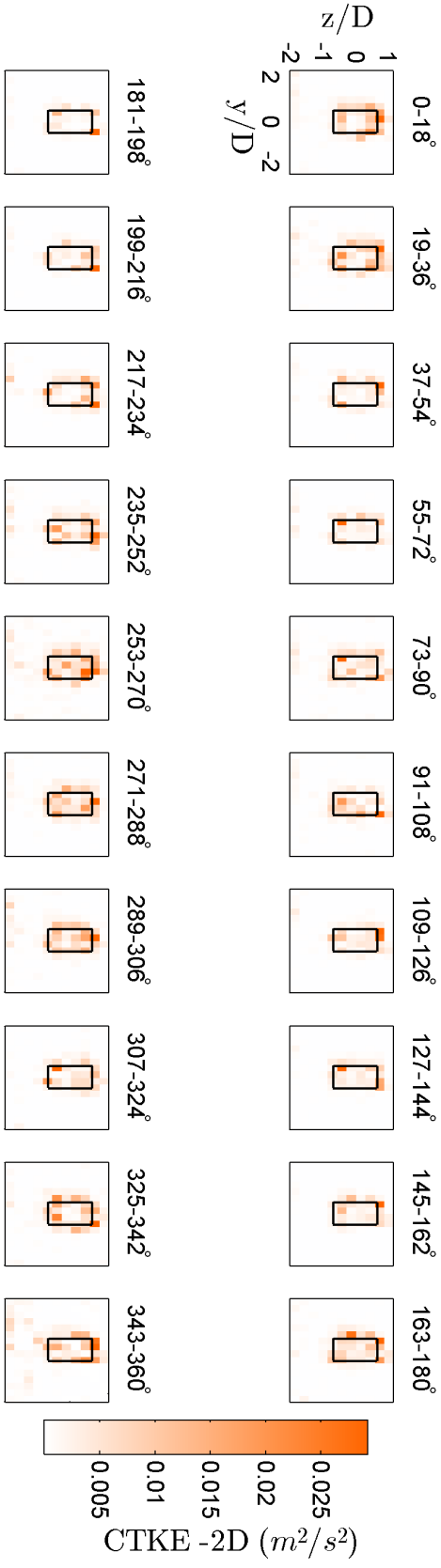

Figure A.6: Phase-locked CTKE at 2 diameters.

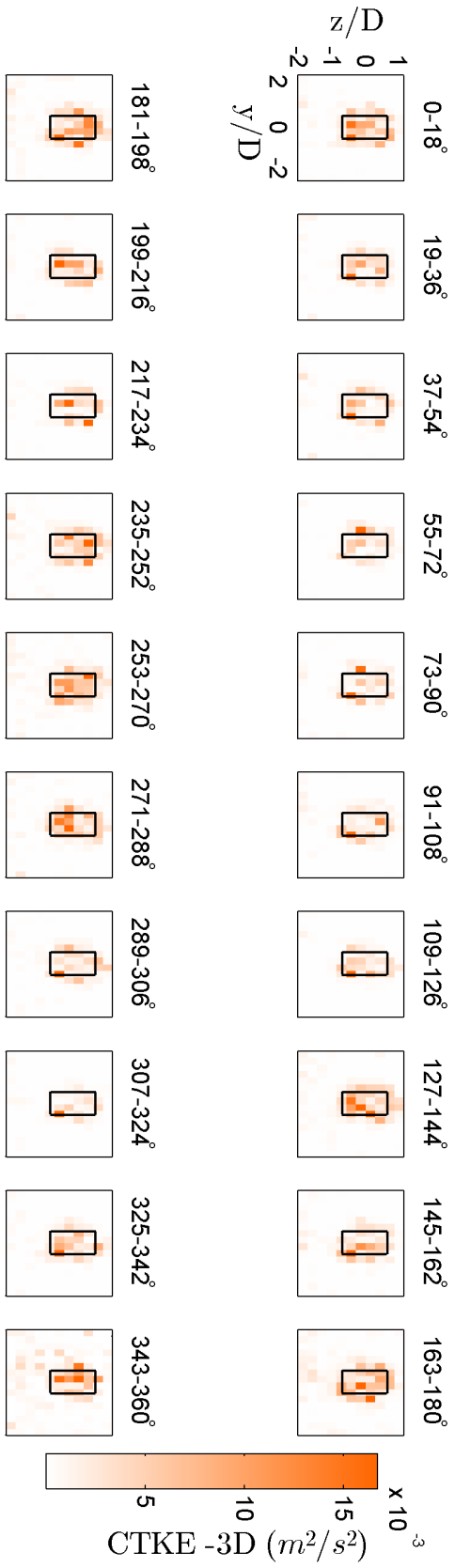

Figure A.7: Phase-locked CTKE at 3 diameters.

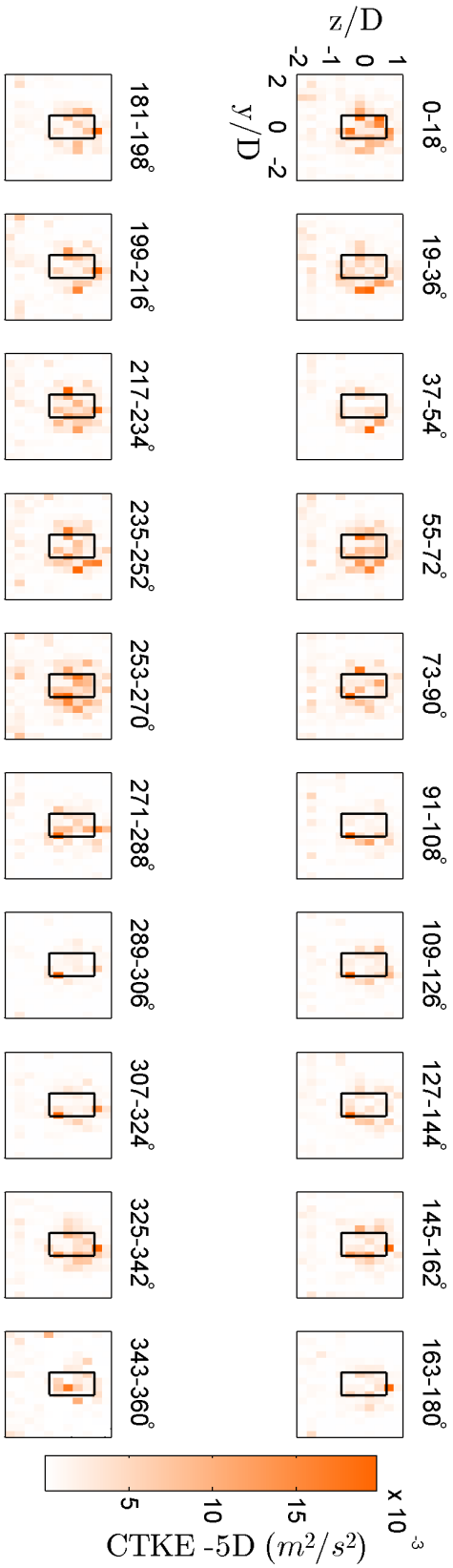

Figure A.8: Phase-locked CTKE at 5 diameters.

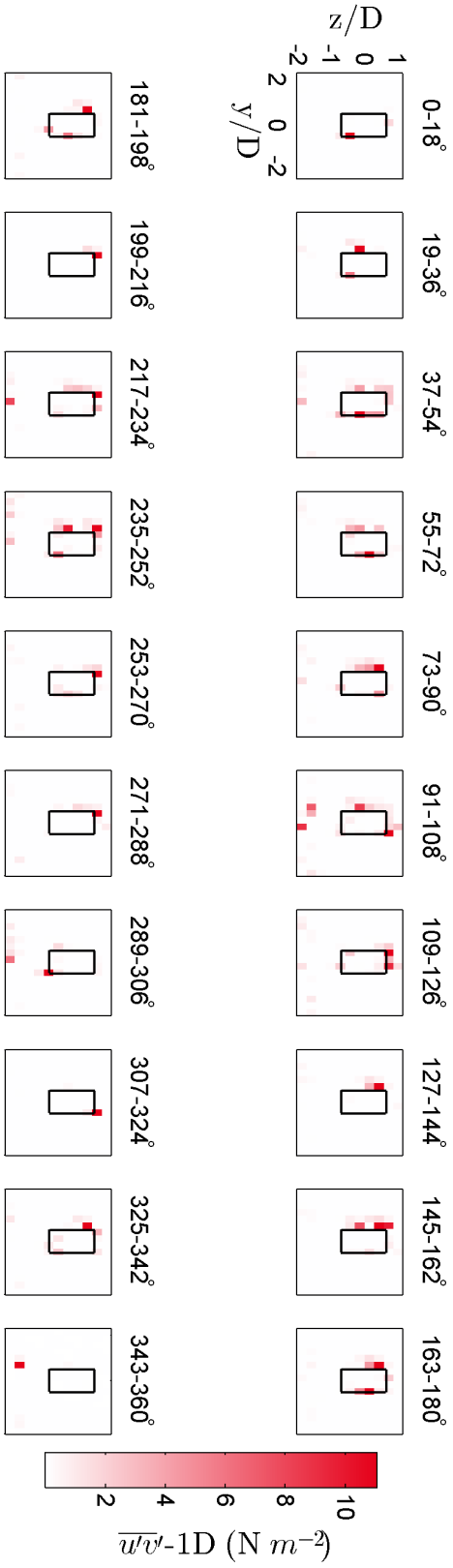

Figure A.9: Phase-locked Reynolds shear stress, $\overline{u'v'}$, at 1 diameter.

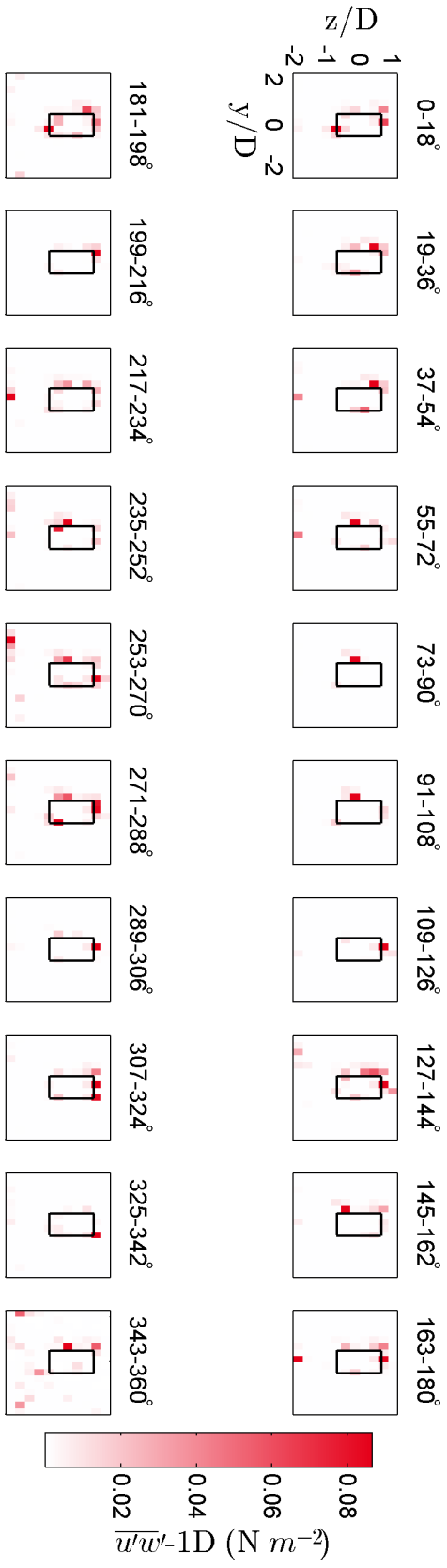

Figure A.10: Phase-locked Reynolds shear stress, $\overline{u'w'}$, at 1 diameter.

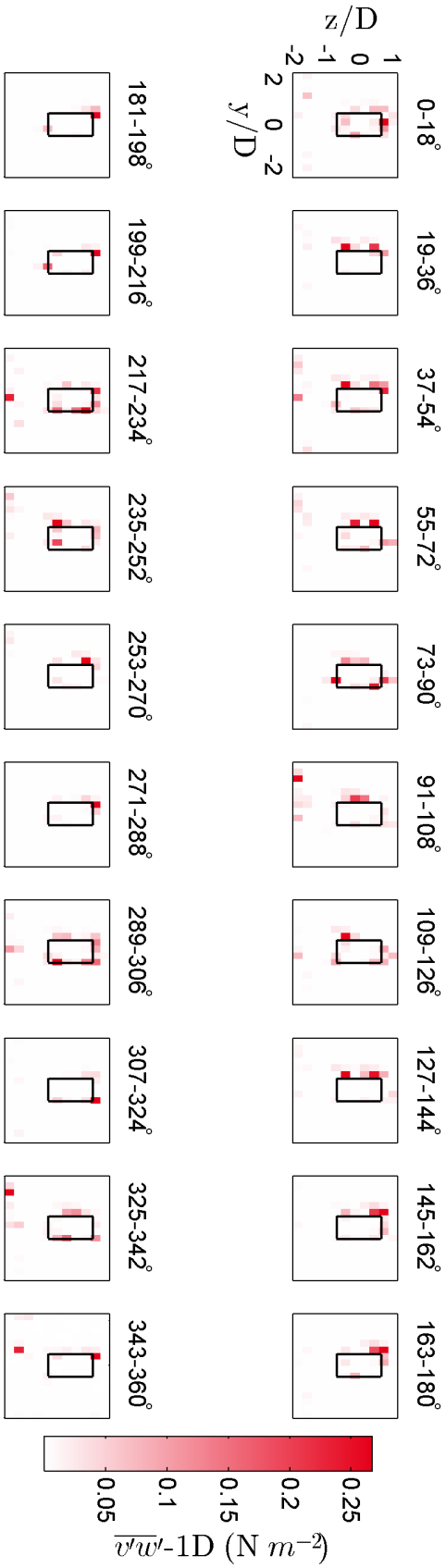

Figure A.11: Phase-locked Reynolds shear stress, $\overline{v'w'}$, at 1 diameter.

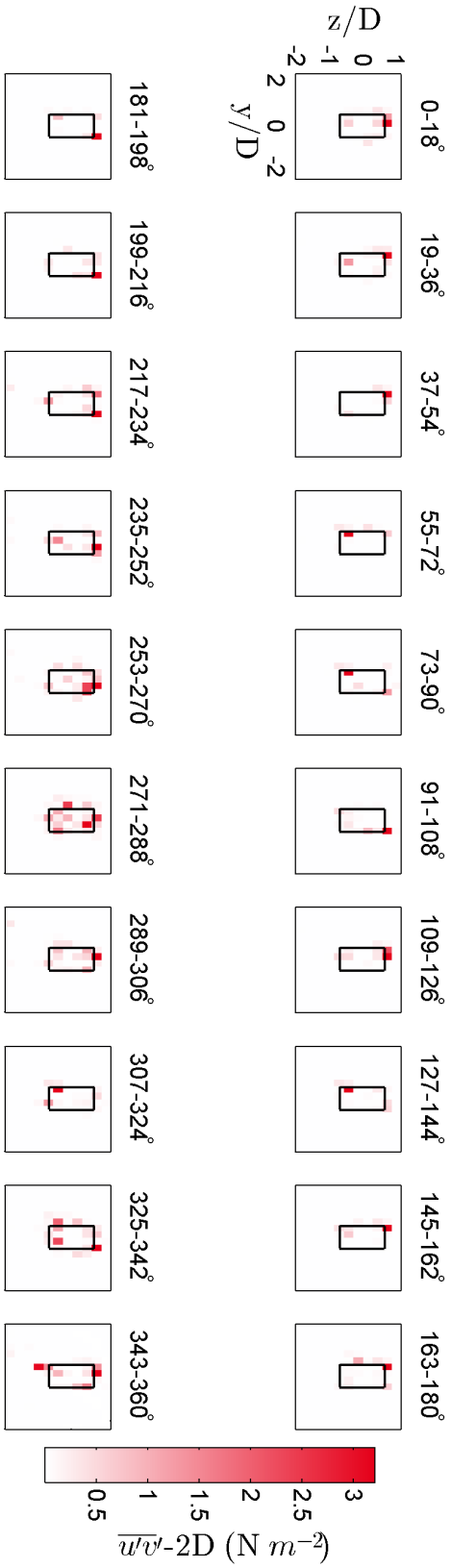

Figure A.12: Phase-locked Reynolds shear stress, $\overline{u'v'}$, at 2 diameters.

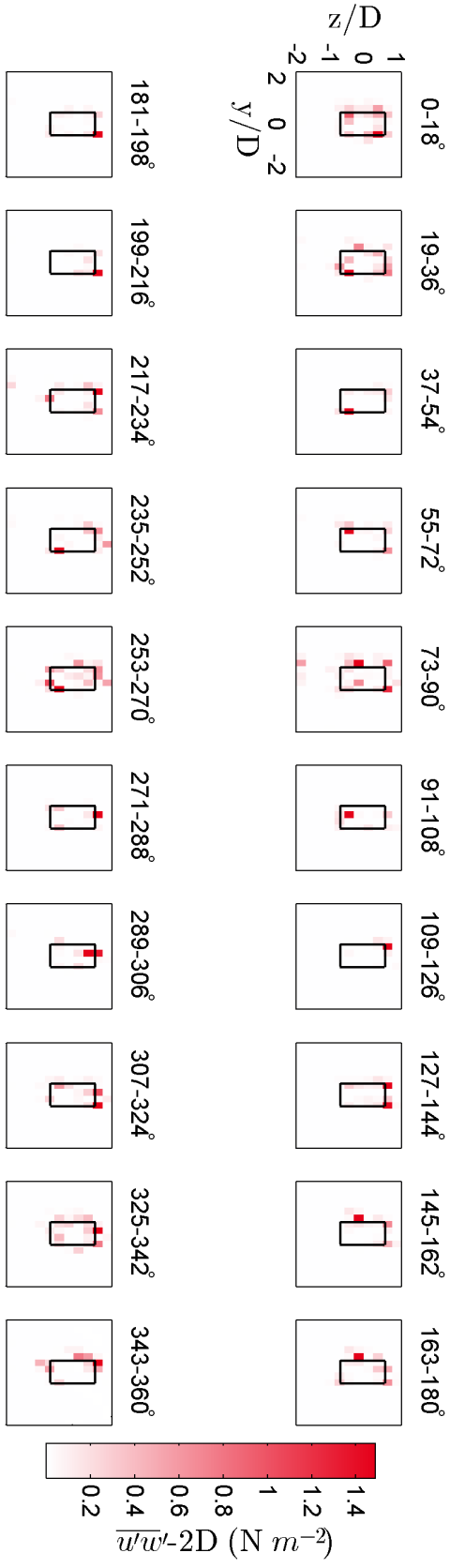

Figure A.13: Phase-locked Reynolds shear stress, $\overline{u'w'}$, at 2 diameters.

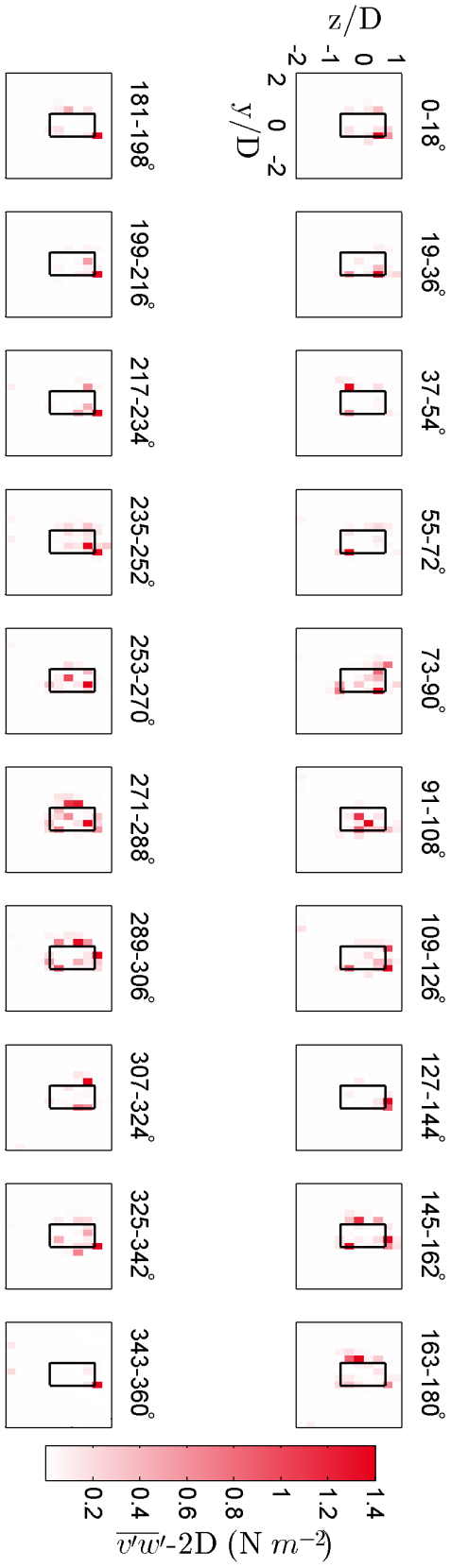

Figure A.14: Phase-locked Reynolds shear stress, $\overline{v'w'}$, at 2 diameters.

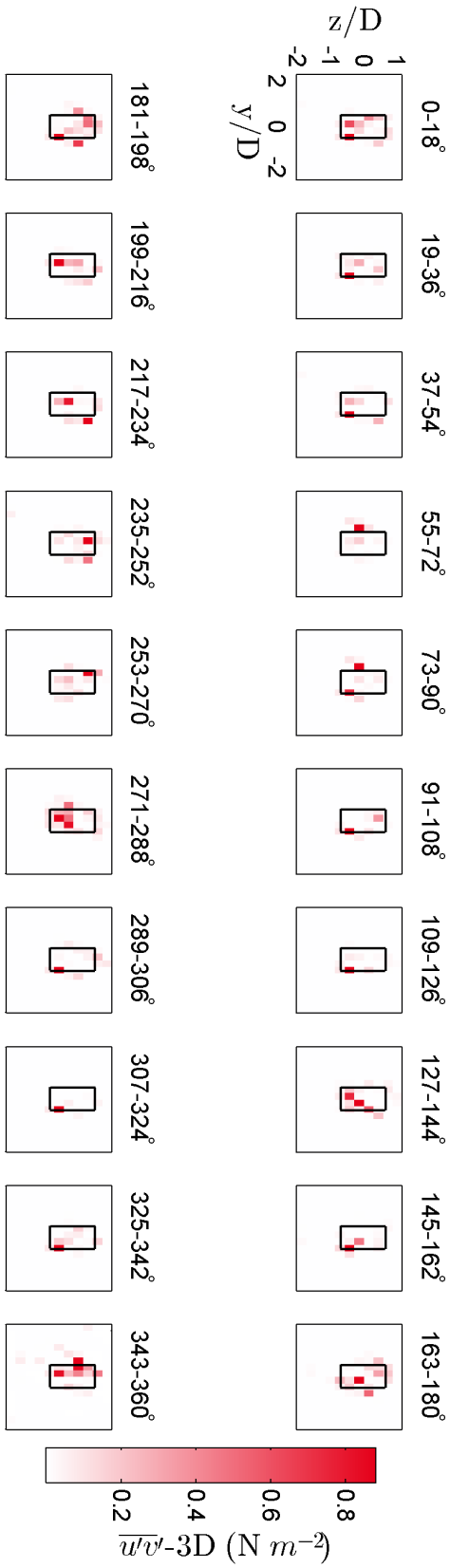

Figure A.15: Phase-locked Reynolds shear stress, $\overline{u'v'}$, at 3 diameters.

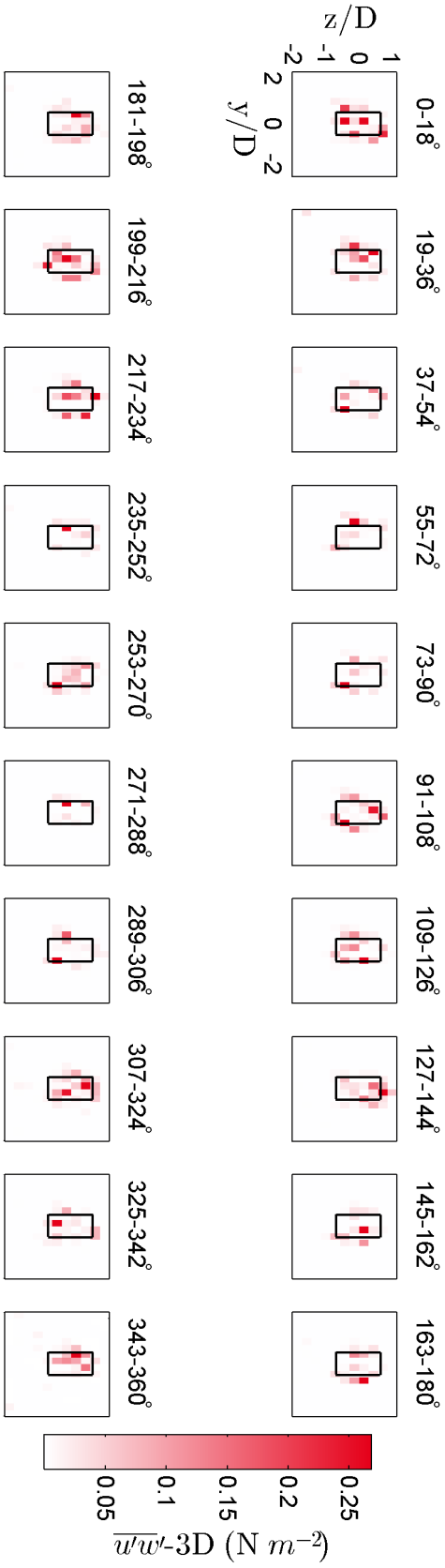

Figure A.16: Phase-locked Reynolds shear stress, $\overline{u'w'}$, at 3 diameters.

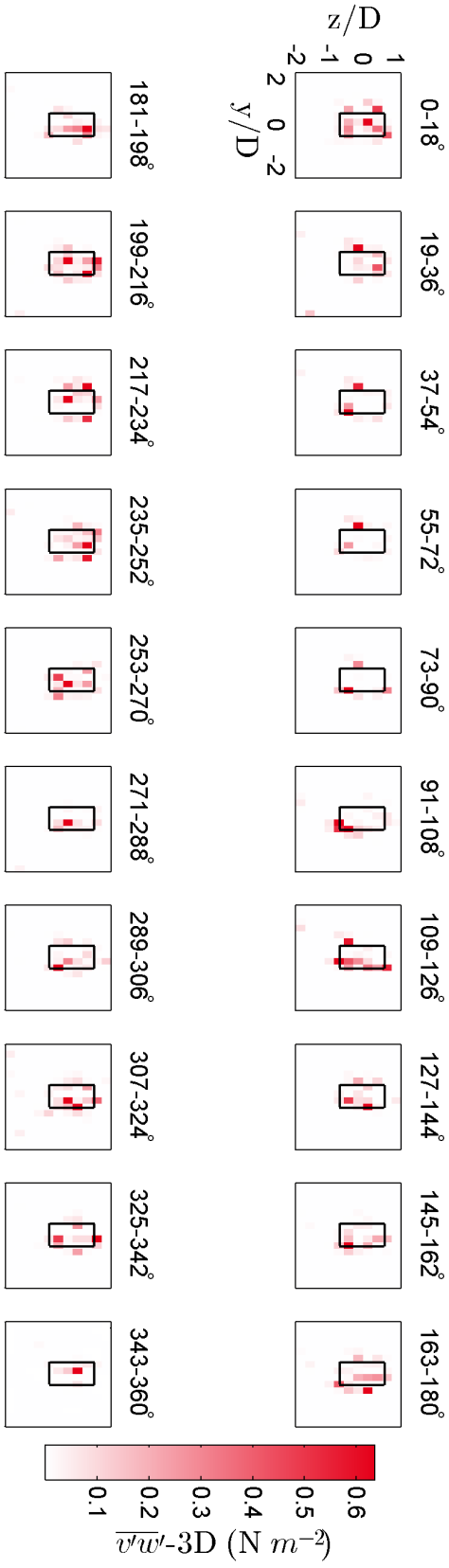

Figure A.17: Phase-locked Reynolds shear stress, $\overline{v'w'}$, at 3 diameters.

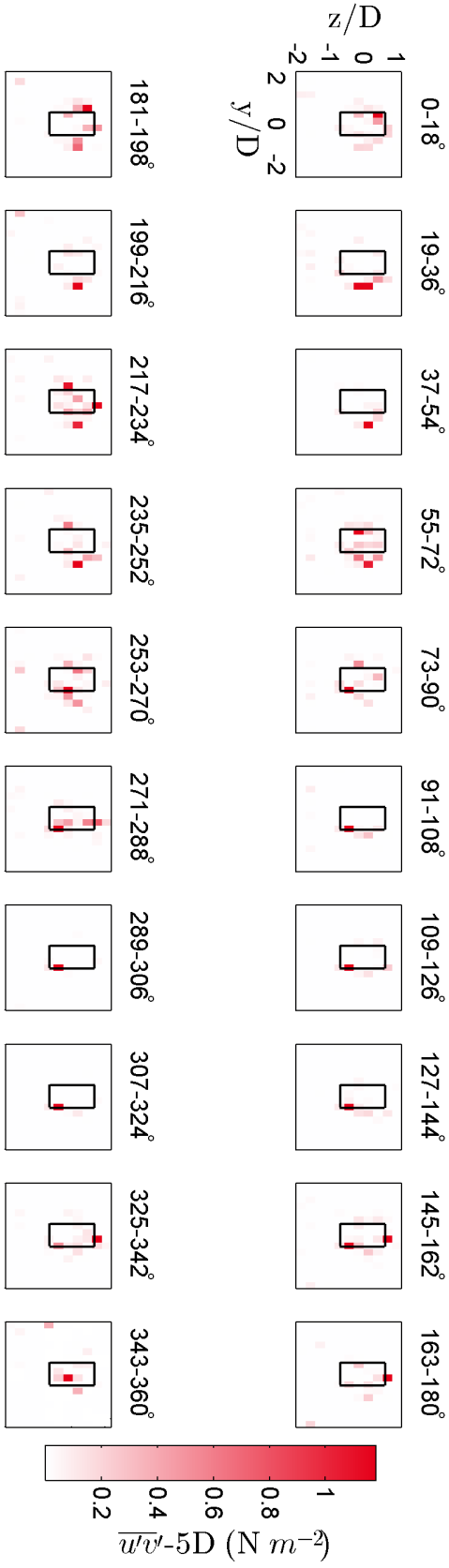

Figure A.18: Phase-locked Reynolds shear stress, $\overline{u'v'}$, at 5 diameters.

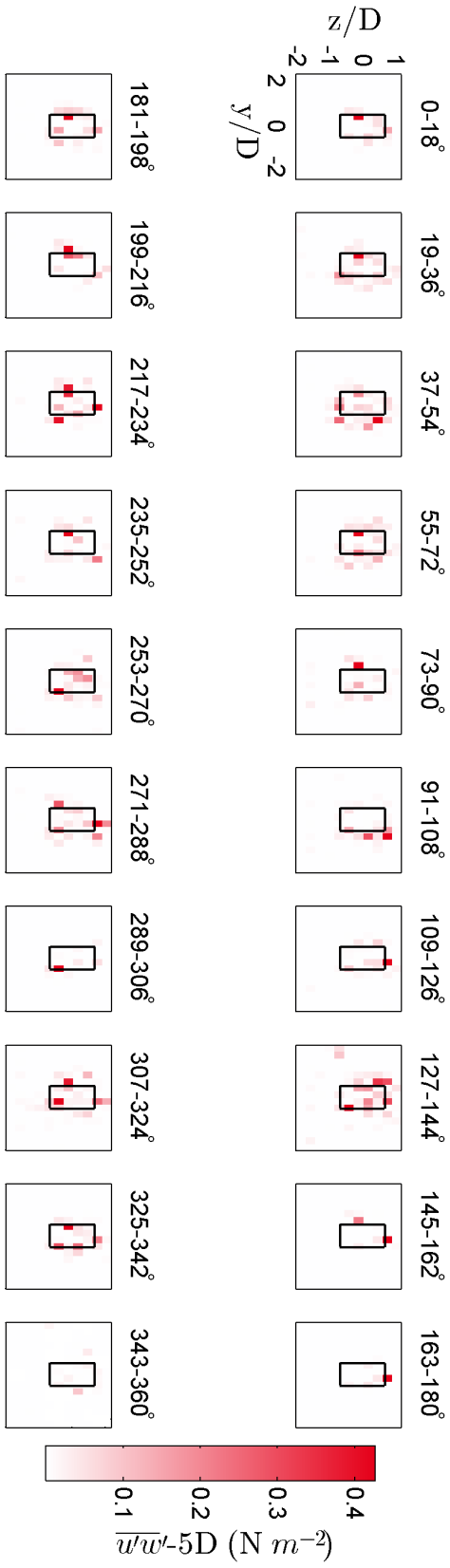

Figure A.19: Phase-locked Reynolds shear stress, $\overline{u'w'}$, at 5 diameters.